All-optical magnetometric characterization of the exchange-coupled antiferromagnet/ferromagnet system $Mn_2Au|Ni_{80}Fe_{20}$ by terahertz spin-orbit torques

Y. Behovits,[1] A. L. Chekhov,[1] B. Rosinus Serrano,[1] A. Ruge,[1] S. Reimers,[2] Y. Lytvynenko,[2,3] M. Kläui,[2] M. Jourdan,[2] and T. Kampfrath[1]

[1]*Department of Physics, Freie Universität Berlin, 14195 Berlin, Germany*
[2]*Institute of Physics, Johannes Gutenberg-Universität Mainz, 55099 Mainz, Germany*
[3]*Institute of Magnetism of the NAS and MES of Ukraine, 03142 Kyiv, Ukraine*

(Received 18 November 2024; revised 19 March 2026; accepted 31 March 2026; published 1 June 2026)

Antiferromagnetic materials have great potential for spintronic applications at terahertz (THz) frequencies. However, in contrast to ferromagnets, experimental investigations of antiferromagnets are often challenging due to a lack of straightforward external control of the Néel vector $\boldsymbol{L}$ and suitable probes. Here, we study an AFM|FM stack consisting of an antiferromagnetic metal layer (AFM) of the novel material Mn_2Au and a ferromagnetic metal layer (FM) of $Ni_{80}Fe_{20}$. To characterize the AFM|FM stack as a function of the quasistatic $\boldsymbol{B}_{ext}$, we perform quasistatic as well as THz-pump magneto-optic probe experiments. Our results demonstrate that AFM and FM are exchange-coupled, and that $\boldsymbol{L}$ of the AFM can be set by the simple application of an external in-plane magnetic field $\boldsymbol{B}_{ext}$. We identify ultrafast signal components that can consistently be explained by the in-plane antiferromagnetic magnon mode excited by fieldlike Néel spin-orbit torque (NSOT). Remarkably, we find that the $\boldsymbol{B}_{ext}$- and THz-pump-induced changes in the optical response of the sample are dominated exclusively by the spin degrees of freedom of AFM. Nonmagnetic signal contributions are minor. We fully calibrate the magnetic circular and magnetic linear optical birefringence of AFM and extract the efficiency of the NSOT. Finally, by selective excitation of domains with different orientations of $\boldsymbol{L}$, we are able to determine the relative volume fraction of 0°, 90°, 180° and 270° domains during the quasistatic reversal of $\boldsymbol{L}$ by $\boldsymbol{B}_{ext}$. Our insights are an important prerequisite for future studies of ultrafast coherent switching of spins by THz NSOT and show that THz-pump magneto-optic-probe experiments are a powerful tool to characterize magnetic properties of antiferromagnets.

DOI: 10.1103/86ds-j6vv

I. INTRODUCTION

Antiferromagnetic spin dynamics has attracted strongly increasing attention in recent years because of its potential to build spintronic devices that are robust against magnetic fields and operate at terahertz (THz) frequencies [1–7]. Importantly, the discovery of Néel spin-orbit torques has opened up possibilities to manipulate antiferromagnetic order by electric currents, in particular in the antiferromagnetic metals Mn_2Au and CuMnAs [8–13]. Remarkably, recent ultrafast THz-pump magneto-optic-probe experiments on Mn_2Au thin films indicate that coherent 90° or even 180° rotation of the Néel vector $\boldsymbol{L}$ through fieldlike Néel spin-orbit torque (NSOT) should be possible if the THz currents in the film can be further increased. Such functionalities would pave the way to THz-rate information writing by NSOT in antiferromagnets [14].

However, ultrafast switching of $\boldsymbol{L}$ has not been observed yet, as it poses a number of challenges: (C1) For experiments, a control parameter is needed that allows us to initialize $\boldsymbol{L}$ in a well-defined state. Here, the robustness of antiferromagnets to external fields is, in fact, a disadvantage and prevents $\boldsymbol{L}$ control in typical laboratory settings. Electric current pulses can provide control over $\boldsymbol{L}$ [13], but they can only be used in patterned and contacted films. (C2) Suitable ultrafast probes are required to detect the instantaneous $\boldsymbol{L}$ and the transient magnetization in the antiferromagnet. In particular, we need to be able to differentiate opposite Néel-vector directions, i.e., $\pm\boldsymbol{L}$, as well as 90°-rotated domains. Protocols to calibrate signals relative to $\boldsymbol{L}$ are highly desired. (C3) The torque on $\boldsymbol{L}$ and, thus, the NSOT-driving THz-pump electric field needs to be increased to overcome the switching barrier.

In this work, we address the challenges (C1) and (C2). To this end, we conduct THz-pump magneto-optic probe experiments [Fig. 1(a)] on an exchange-coupled AFM|FM stack, with an antiferromagnetic metal layer AFM of Mn_2Au and a ferromagnetic metal layer FM of $Ni_{80}Fe_{20}$ (permalloy Py) [15,16]. Importantly, we confirm that the FM magnetization can be used to control the $\boldsymbol{L}$ landscape of AFM, thereby overcoming challenge (C1). We characterize the Néel vector $\boldsymbol{L}$ and the magnetization $\boldsymbol{M}^{AFM}$ of the AFM in Mn_2Au|Py by all-optical probes, both in the quasistatic and the ultrafast regime. We find that magnetic signal contributions dominate the optical response and that probes linear and quadratic in the order parameters give direct insight into antiferromagnetic spin

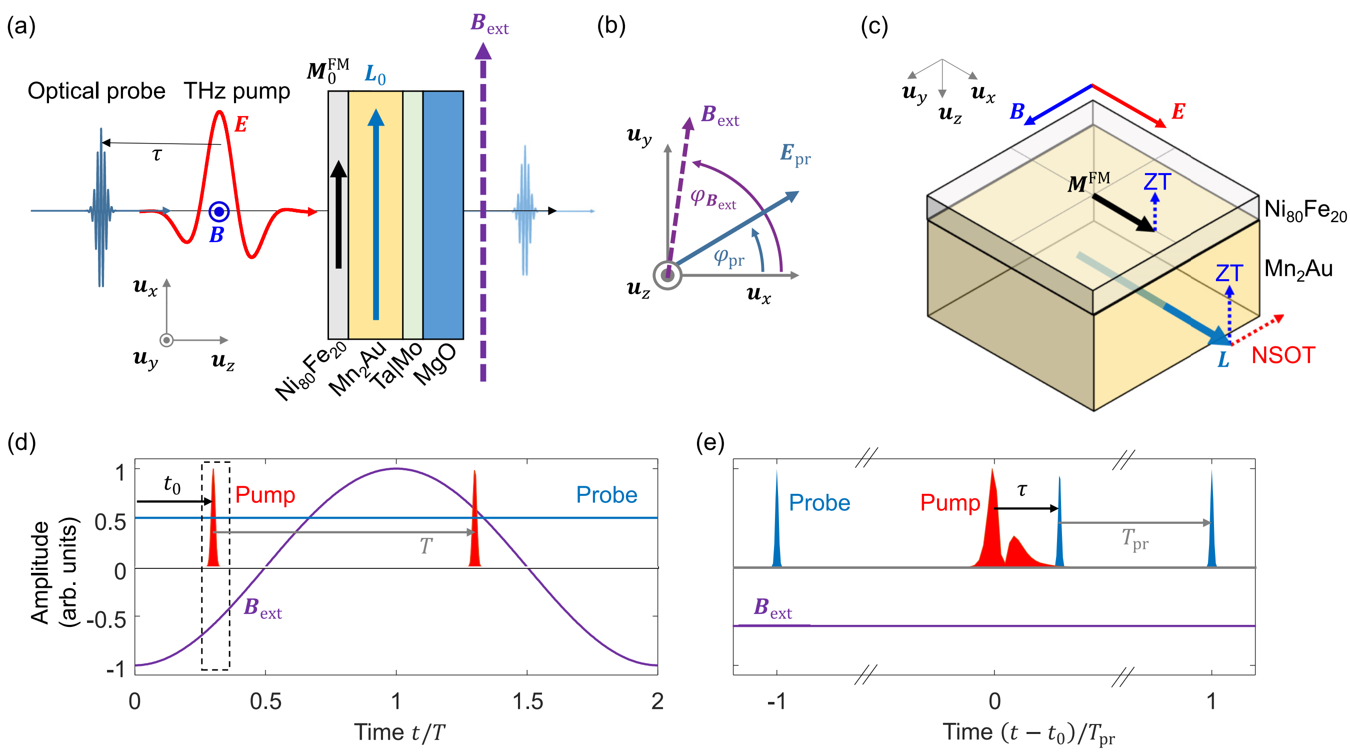

FIG. 1. Schematic of experiment and torque-driven dynamics. (a) Schematic of the experiment. A THz pump pulse is incident on the sample, and the resulting spin dynamics is interrogated by an optical probe through magneto-optic effects. The sample is a thin-film stack sub||seed|AFM|FM, where the substrate slab (sub) is MgO(500 μm), the seed layer is Mo(20 nm)|Ta(13 nm), the antiferromagnetic metal layer AFM is Mn_2Au(50 nm), and the ferromagnetic metal layer FM is $Ni_{80}Fe_{20}$(10 nm). (b) Definition of the probe polarization angle $\varphi_{\mathrm{pr}} = \sphericalangle(\boldsymbol{E}_{\mathrm{pr}}, \boldsymbol{u}_x)$, where $\boldsymbol{E}_{\mathrm{pr}}$ is the probe electric field and $\varphi_{B_{\mathrm{ext}}}$ the angle of the external magnetic field $\boldsymbol{B}_{\mathrm{ext}}$. (c) Possible fieldlike Zeeman torque (ZT) and Néel spin-orbit torque (NSOT) on layers FM and AFM with magnetic order parameters $\boldsymbol{M}^{\mathrm{FM}}$ and $\boldsymbol{M}^{\mathrm{AFM}}$, $\boldsymbol{L}$, respectively. (d) Timing diagram of one cycle of the stroboscopic measurement, i.e., for time t between 0 and $2T$, where $T = 1$ ms. The purple line shows the external magnetic field $\boldsymbol{B}_{\mathrm{ext}}(t)$ with a period of $2T$. The THz pump pulses (red; duration exaggerated) arrive with repetition period T at times t_0 and $t_0 + T$ relative to the magnetic-field minimum $-\boldsymbol{B}_{\mathrm{ext0}}$. The probe pulses are spaced equidistantly by the repetition period $T_{\mathrm{pr}} = 12.5$ ns $\ll T$ and arrive quasicontinuously. (e) Magnified view of the dashed-line box in (d). It shows the THz pump-pulse energy density $\propto \boldsymbol{E}^2(t)$ (red), and a probe pulse (blue) that arrives with a delay τ after the pump. One preceding and one subsequent probe pulse at time $t_0 + \tau \pm T_{\mathrm{pr}}$ are shown, too. On the timescale $|\tau| \ll T$ of the pump-probe experiment, $\boldsymbol{B}_{\mathrm{ext}}$ is approximately constant.

dynamics, thereby resolving challenge (C2). In particular, we show that, with these probes, the Néel spin-orbit torkance and the volume fractions of the four in-plane $\boldsymbol{L}$ domains can be inferred. Signal contributions from dynamic changes in the FM magnetization $\boldsymbol{M}^{\mathrm{FM}}$ are minor. Therefore, once challenge (C3) is solved, the way to NSOT-driven ultrafast antiferromagnetic-order switching is open.

II. EXPERIMENTAL SETUP

A schematic of our experimental approach is shown in Figs. 1(a)–1(c). In brief, our sample is a Mn_2Au|Py stack. The Py magnetization $\boldsymbol{M}^{\mathrm{FM}}$ and, thus, Néel vector $\boldsymbol{L}$ of the exchange-coupled Mn_2Au is set by a quasistatic external magnetic field $\boldsymbol{B}_{\mathrm{ext}}$ that is varied quasistatically as a function of time t.

To apply ultrafast NSOT, a THz pump pulse is normally incident onto the sample stack. After a delay τ, the sample state is interrogated by a normally incident and linearly polarized optical probe pulse (wavelength 800 nm, duration ≈15 fs). We use identical probe pulses to also characterize the unperturbed sample in the absence of a pump pulse, in particular as a function of $\boldsymbol{B}_{\mathrm{ext}}$. On one occasion, we take advantage of probe pulses under nonnormal incidence.

In the following, we describe our experiment in more detail.

A. Samples and external magnetic field

The AFM|FM samples consist of an antiferromagnetic metal layer AFM and a ferromagnetic metal layer FM [Fig. 1(a)]. For the primary sample, the AFM is Mn_2Au(001)(50 nm) and grown epitaxially on Ta(001)(13 nm)|Mo(001)(20 nm) double buffer layers on MgO(100) substrates by magnetron sputtering, as described in detail in Ref. [16]. A polycrystalline FM of Py with a thickness of 10 nm is deposited on top of the Mn_2Au at room temperature, followed by a polycrystalline capping layer SiN_x(2 nm) to protect the metallic stack from oxidation. For comparison, we use samples with varied composition (Fig. S2 [17]). Unless noted otherwise, all measurements in the main text are performed on the primary sample, which has lateral dimensions of 10 × 5 mm^2 and a nominal metal-film thickness of 93 nm. Its DC sheet resistance is determined

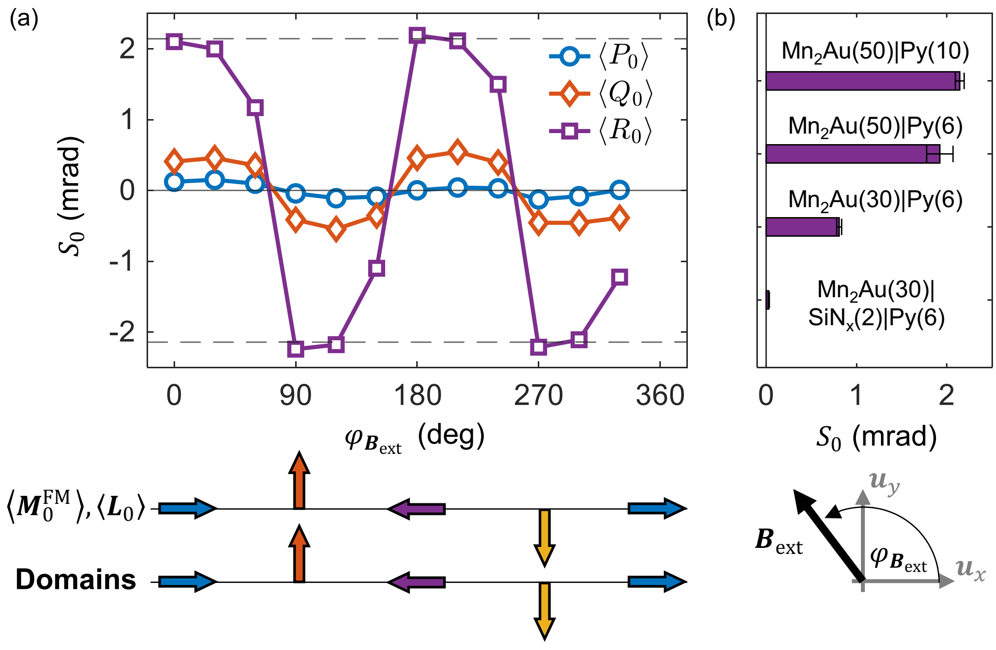

FIG. 2. Magneto-optic signals vs direction of the quasistatic external magnetic field $\boldsymbol{B}_{\mathrm{ext}}$. (a) Probe-polarization rotation S_0 vs azimuthal angle $\varphi_{\boldsymbol{B}_{\mathrm{ext}}}$ of the static in-plane magnetic field $\boldsymbol{B}_{\mathrm{ext}} = -B_{\mathrm{ext0}}(\cos\varphi_{\boldsymbol{B}_{\mathrm{ext}}}\boldsymbol{u}_x + \sin\varphi_{\boldsymbol{B}_{\mathrm{ext}}}\boldsymbol{u}_y)$ (see bottom-right schematic). The components $\langle P_0\rangle$, $\langle Q_0\rangle$, $\langle R_0\rangle$ of signal S_0 are extracted according to Eq. (5) from four linear polarization angles (Appendixes A 3 and B 1 and Fig. S2 [17]). The mean signal is set to zero. The first bottom schematic displays expected orientations of the volume-averaged magnetization $\langle \boldsymbol{M}_0^{\mathrm{FM}}\rangle$ of layer FM ($Ni_{80}Fe_{20}$, i.e., permalloy Py) and the Néel vector $\langle \boldsymbol{L}_0\rangle$ of layer AFM (Mn_2Au) at $\varphi_{\boldsymbol{B}_{\mathrm{ext}}} = 0^\circ,\ 90^\circ,\ 180^\circ$ and 270°. It is consistent with the data of (a). The second bottom schematic displays the expected statistics of the local $\boldsymbol{L}_0$, assuming saturation by $\boldsymbol{B}_{\mathrm{ext}}$. The AFM|FM stack is Mn_2Au(50 nm)|Py(10 nm). (b) Peak amplitude of signal component $\langle R_0\rangle$ for different modifications of the AFM|FM stack. Numbers in parentheses indicate layer thickness in nanometers.

to be 1.2 Ω by a four-point-probe measurement (Ossila Four-Point Probe), corresponding to a thickness-averaged conductivity of 8.8 MS m^{-1}.

To set the external magnetic field $\boldsymbol{B}_{\mathrm{ext}}$ parallel to the sample plane, we use two methods, which are dedicated to controlling the direction and amplitude of $\boldsymbol{B}_{\mathrm{ext}}$ (Figs. 2 and 3). With the first method, we generate a static magnetic field $\boldsymbol{B}_{\mathrm{ext}}$ by a pair of permanent magnets with magnitude $B_{\mathrm{ext0}} = 0.35$ T. By mounting the magnets on a mechanical rotation stage, we can set the azimuthal angle $\varphi_{\boldsymbol{B}_{\mathrm{ext}}}$ of the magnetic field prior to each measurement. Therefore, $\boldsymbol{B}_{\mathrm{ext}}$ remains constant over the duration of the measurement and equals

$$\boldsymbol{B}_{\mathrm{ext}} = B_{\mathrm{ext0}}(\cos\varphi_{\boldsymbol{B}_{\mathrm{ext}}}\boldsymbol{u}_x + \sin\varphi_{\boldsymbol{B}_{\mathrm{ext}}}\boldsymbol{u}_y). \tag{1}$$

With the second method, an electromagnet generates a magnetic field along $\boldsymbol{u}_x$ whose amplitude varies harmonically with time t. Consequently, we have

$$\boldsymbol{B}_{\mathrm{ext}}(t) = B_{\mathrm{ext}}(t)\boldsymbol{u}_x \quad \text{with} \quad B_{\mathrm{ext}}(t) = -B_{\mathrm{ext0}}\cos\frac{2\pi t}{2T}, \tag{2}$$

where the maximum field is $B_{\mathrm{ext0}} = 0.19$ T. The period is chosen to be twice the time $T = 1$ ms between two consecutive pump pulses. This choice allows us to rapidly conduct pump-probe measurement for positive and negative magnetic field because $B_{\mathrm{ext}}(t+T) = -B_{\mathrm{ext}}(t)$.

B. Pump and probe details

The THz pump and optical probe pulses are derived from an amplified Ti:sapphire laser system. It is fed by nanojoule-class pulses from a Ti:sapphire laser oscillator, resulting in millijoule-class pulses with an accordingly lower repetition rate. The pump pulses are derived from the amplified laser pulses (repetition rate $1/T = 1$ kHz), whereas the probe pulses are taken from part of the seed-laser beam (repetition rate $1/T_{\mathrm{pr}} = 80$ MHz).

1. Pump pulses

The THz pump pulses are generated by excitation of a large-area Si-based spintronic THz emitter (STE, T-Spin2X, TeraSpinTec GmbH) [18] with amplified laser pulses (pulse energy 7 mJ, center wavelength 800 nm, duration 40 fs). The pump-beam diameter of 34 mm (intensity 1/e^2) results in a THz beam with a diameter of 24 mm (intensity 1/e^2). A 90° off-axis parabolic mirror focuses the THz beam onto the sample surface with a focus diameter that decreases as $1/\omega$ with frequency $\omega/2\pi$ and equals 1 mm (intensity 1/e^2) at 1 THz. The focus diameter is determined with a microbolometer array (Xenics Gobi 640+).

The focal incident THz electric field is measured by Zeeman-torque sampling (Fig. S1 [17]) [19] and amplitude calibration through a GaP window. We reach peak electric and magnetic fields of approximately 1.4 MVcm^{-1} and 0.5 T, respectively.

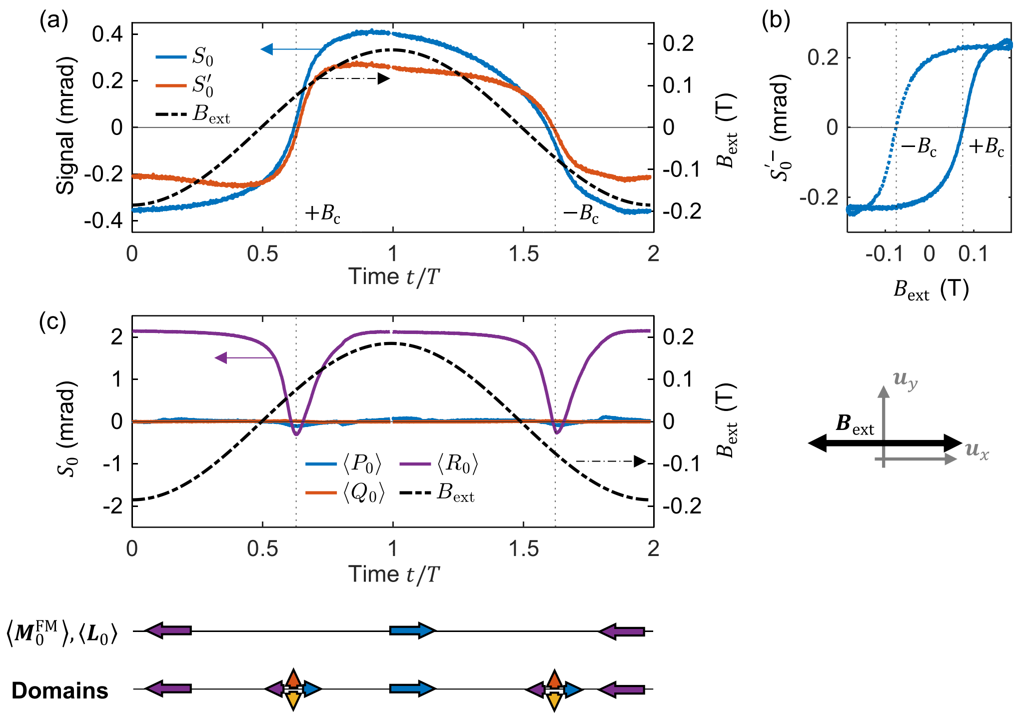

FIG. 3. Magneto-optic signal vs magnitude of the quasistatic external magnetic field $\boldsymbol{B}_{ext}$. (a) Signal S_0 (blue line) and amplitude B_{ext} (black line) of the quasistatic external magnetic field $\boldsymbol{B}_{ext} = B_{ext}\boldsymbol{u}_x$ vs time t over one cycle of B_{ext} (see schematic at bottom-right side). The probe has an angle of incidence of 30° to maximize MCB, and it is p-polarized, i.e., perpendicular to $\boldsymbol{u}_y$, to minimize MLB. The signal S_0' (red line) is S_0 minus a rescaled version of B_{ext} to remove the MCB of the substrate (Fig. S3 [17]). (b) Signal $S_0'^-$ vs B_{ext}, where $S_0'^-$ is signal S_0' from (a), but only the component odd with respect to $\boldsymbol{B}_{ext}$ [Fig. S3 [17] and Eq. (8)]. Dashed vertical lines indicate the coercive field of $B_c \approx 75$ mT, which is also displayed in (a). (c) Components of signal $S_0(t)$ [Eq. (5)] vs time t, where $\boldsymbol{B}_{ext}(t) = B_{ext}(t)\boldsymbol{u}_x$ (black line) varies quasistatically. The probe angle of incidence is 0°. Components $\langle P_0 \rangle$, $\langle Q_0 \rangle$, and $\langle R_0 \rangle$ are extracted according to Eq. (5) from eight linear probe-polarization angles (Fig. S4 [17]). For $\langle P_0 \rangle$ and $\langle Q_0 \rangle$, the signal is set to zero for $t = 0$. For $\langle R_0 \rangle$, the amplitude at $t = 0$ is set to the maximum value of the corresponding signal in Fig. 2(a). This procedure assumes that $\langle \boldsymbol{M}_0^{FM} \rangle$ and $\langle \boldsymbol{L}_0 \rangle$ are saturated by $\boldsymbol{B}_{ext}$. The first bottom schematic shows orientations of the volume-averaged $\langle \boldsymbol{M}_0^{FM} \rangle$ and $\langle \boldsymbol{L}_0 \rangle$ at various points in time, which are consistent with the data of (b). The second bottom schematic displays the expected distribution of the local $\boldsymbol{L}_0$ over four domains. At $t/T \approx 0.6$ (dashed vertical line), where $B_{ext} \approx +B_c$, a multi-domain state is expected. Here, $\langle \boldsymbol{M}_0^{FM} \rangle$ and $\langle \boldsymbol{L}_0 \rangle$ vanish, and the domains are equally populated, as indicated by the four arrows.

The STE offers several features that are helpful in our experiment. First, its collinear geometry permits straightforward alignment. Second, it provides THz pulses with a short duration <250 fs, which eases the separation of different signal contributions based on their potentially different timescales. Finally, we can accurately control the polarization plane and field polarity of the THz field by simply rotating the static magnetic field that sets the magnetization of the STE [18].

2. *Signal probing*

The probe beam is normally incident onto the sample and focused to a diameter of 30 μm (intensity $1/e^2$) at the sample surface. After a probe pulse has traversed the sample, we measure changes S in the probe polarization, i.e., the rotation of the probe polarization plane and the ellipticity. To detect the probe rotation, we employ a combination of a half-wave plate, a polarizing beam splitter and a pair of balanced photodiodes (Appendix A). To detect the probe ellipticity, we convert the ellipticity to rotation by introducing a quarter-wave plate before the half-wave plate.

We note that the signal S is always subject to an unknown offset due, e.g., to static birefringence of the substrate or slow setup drifts. Therefore, only changes in S due, e.g., to the pump pulse or variations of the external magnetic field can be measured. The signal can be written as

$$S(t) = S_0(t) + \Delta S(t), \tag{3}$$

where $S_0(t)$ is the slowly varying signal due to quasistatic variations of $\boldsymbol{B}_{ext}$ versus probe time t. The pump-induced signal $\Delta S(t)$ typically varies on much shorter timescales due to the impact of the pump pulse.

Importantly, the probe pulses are derived from the seed oscillator of the laser system, which offers advantages relative to probe pulses from the amplified pulse train [20]. First, they exhibit significantly reduced pulse-to-pulse variations and smaller pulse duration. Second, their about 80 000 times higher repetition rate allows us to densely sample the signal $S(t)$ at times

$$t = t_{pu} + nT_{pr} + \tau. \tag{4}$$

Here, t_{pu} is the arrival time of the pump. To detect the ultrafast pump-induced variations of signal $S(t)$, the fine delay τ can be set between −400 and +400 ps in steps of about 20 fs by a retroreflector and a mechanical translation stage that is traversed by the probe beam. Slower variations of $S(t)$

TABLE I. Table of symmetry-allowed signal components P, Q and R for normally incident probe beam [Eq. (5)]. $\boldsymbol{L}$ is only present in the antiferromagnetic layer, while $\boldsymbol{M}$ is generally present in both ferromagnetic and antiferromagnetic layers. The coefficients $p_{\boldsymbol{M}}(\boldsymbol{r})$, $q_{\boldsymbol{L}}(\boldsymbol{r})$, $\boldsymbol{q_M}(\boldsymbol{r})$, $r_{\boldsymbol{L}}(\boldsymbol{r})$, and $r_{\boldsymbol{M}}(\boldsymbol{r})$ quantify the sensitivity to the local $\boldsymbol{L}(\boldsymbol{r})$ and $\boldsymbol{M}(\boldsymbol{r})$ at position $r = (x, y, z)$ and scale with the sample thickness. The total signal $\langle X\rangle$ arises from the weighted average of $X = P,\ Q$ and R over the probed volume V [Eq. (A10)]. For non-normal probe incidence ($\boldsymbol{u}_{\mathrm{pr}} \neq \boldsymbol{u}_z$), the situation changes. For example, $\boldsymbol{P}_{\mathcal{S}}$ becomes proportional to the projection $\boldsymbol{M}\cdot\boldsymbol{u}_{\mathrm{pr}}$ of the magnetization on the probe-propagation direction.

Com-ponent	Type	Related φ_{pr} dependence	Contribution due to changes exclusively in spin degrees of freedom $\mathcal{S}$	Nonspin contribution
P	MCB	1	$P_{\mathcal{S}} = p_{\boldsymbol{M}} M_z$	$P_{\mathcal{N}} = P - P_{\mathcal{S}}$
Q	MLB	$\cos(2\varphi_{\mathrm{pr}})$	$Q_{\mathcal{S}} = 2q_{\boldsymbol{L}} L_x L_y + 2q_{\boldsymbol{M}} M_x M_y$	$Q_{\mathcal{N}} = Q - Q_{\mathcal{S}}$
			$= q_{\boldsymbol{L}} L_{\parallel 0}^2 \sin(2\varphi_{\boldsymbol{L}}) + q_{\boldsymbol{M}} M_{\parallel 0}^2 \sin(2\varphi_{\boldsymbol{M}})$	
R	MLB	$\sin(2\varphi_{\mathrm{pr}})$	$R_{\mathcal{S}} = r_{\boldsymbol{L}}(L_x^2 - L_y^2) + r_{\boldsymbol{M}}(M_x^2 - M_y^2)$	$R_{\mathcal{N}} = R - R_{\mathcal{S}}$
			$= r_{\boldsymbol{L}} L_{\parallel 0}^2 \cos(2\varphi_{\boldsymbol{L}}) + r_{\boldsymbol{M}} M_{\parallel 0}^2 \cos(2\varphi_{\boldsymbol{M}})$	

are sampled by the subsequent probe pulses that arrive after delays of nT_{pr}, where n is an integer, and $T_{\mathrm{pr}} \approx T/80\,000 = 12.5$ ns is the time between consecutive probe pulses.

To detect the photodiode signal $S(t)$ of each probe pulse [Eq. (4)] separately, we employ a sufficiently fast digitizer (National Instruments PCI-5122, sampling rate $1/T_{\mathrm{pr}} = 80$ MHz).

3. Pump and probe timing

Figures 1(d) and 1(e) schematically summarize the timing of the experiment. As the signal $S(t)$ repeats periodically with period $2T$, we only need to consider the time interval from 0 to $2T$: First, the pump arrives periodically with period $T = 1$ ms, i.e., at times $t_{\mathrm{pu}} = t_0$ and $t_{\mathrm{pu}} = t_0 + T$, where t_0 is an offset.

Second, the amplitude $B_{\mathrm{ext}}(t)$ of the external magnetic field $\boldsymbol{B}_{\mathrm{ext}}(t) = B_{\mathrm{ext}}(t)\boldsymbol{u}_x$ is cycled with a period of $2T$. Due to the doubled period time, consecutive pump pulses perturb the sample at exactly opposite magnetic fields because $B_{\mathrm{ext}}(t+T) = -B_{\mathrm{ext}}(t)$. Owing to the fast modulation of the magnetic field, we can measure the sample response to fields $\pm\boldsymbol{B}_{\mathrm{ext}}$ with an excellent signal-to-noise ratio. The offset t_0 is straightforwardly controlled by an according phase shift of the periodic $B_{\mathrm{ext}}(t)$.

Third, the probe beam samples $S(t)$ densely at times given by Eq. (4). Note that signal $S_0(t)$ is slow, i.e., $S_0(t+\tau) = S_0(t)$ to a very good approximation because $B_{\mathrm{ext}}(t+\tau) = B_{\mathrm{ext}}(t)$ and $|\tau| \ll T$.

C. Signal phenomenology

1. Normal probe incidence

As shown in Appendix A, the signals obtained for a normally incident probe pulse with linear polarization [14] obey the relationship

$$S \propto \langle P\rangle + \langle Q\rangle \cos(2\varphi_{\mathrm{pr}}) + \langle R\rangle \sin(2\varphi_{\mathrm{pr}}). \tag{5}$$

Each signal term P, Q, and R stems from a combination of elements of the optical conductivity tensor and has a distinctly different dependence on the polarization-plane angle φ_{pr} of the incident probe pulse [Fig. 1(b)]. As summarized in Table I, P, Q and R carry complementary information about the magnetic order in layer AFM and FM.

The angular bracket $\langle . \rangle$ in Eq. (5) denotes averaging over the area and the spectrum of the probe spot and a weighted integration over the thickness of the AFM|FM stack [Appendix A 3, Eq. (A10)]. For example, $\langle P\rangle$ is proportional to the (x, y)-averaged and z-integrated local signal P [Figs. 1(a)–1(c)], where the z integration takes the different probing sensitivity to the magnetic order in Mn_2Au and Py into account (Table I). In the experiment, we focus on variations of $\langle P\rangle$, $\langle Q\rangle$, $\langle R\rangle$ induced by changes in the external magnetic field and/or the THz pump pulse.

The observables $P = P_{\mathcal{S}} + P_{\mathcal{N}}$, $Q = Q_{\mathcal{S}} + Q_{\mathcal{N}}$, and $R = R_{\mathcal{S}} + R_{\mathcal{N}}$ have contributions whose variations solely report on the changes in the spin degrees of freedom $\mathcal{S}$, but also contributions due to variations of the nonspin degrees of freedom $\mathcal{N}$ [14]. According to the probe-polarization dependence of Eq. (5), $P_{\mathcal{S}}$ denotes magnetic circular birefringence (MCB), while $Q_{\mathcal{S}}$ and $R_{\mathcal{S}}$ are referred to as magnetic linear birefringence (MLB). An expansion up to second order in the Néel vector $\boldsymbol{L}$ and magnetization $\boldsymbol{M}$ at position $\boldsymbol{r} = (x, y, z)$ [Figs. 1(a)–1(c)] allows one to derive relationships between $P_{\mathcal{S}}$, $Q_{\mathcal{S}}$, and $R_{\mathcal{S}}$ and the local magnetic order parameters of the Mn_2Au|Py stack. Table I shows how the Néel vector $\boldsymbol{L}(\boldsymbol{r})$, which is present only in the AFM, and the magnetization $\boldsymbol{M}(\boldsymbol{r})$, which has parts $\boldsymbol{M}^{\mathrm{AFM}}$ and $\boldsymbol{M}^{\mathrm{FM}}$ in both AFM and FM, contribute to the signal. MCB and MLB report on the order parameters to linear and quadratic order, respectively. Table I relies on the assumption that only the bulk properties of tetragonal Mn_2Au and isotropic Py are relevant.

Changes in the non-spin-related components $P_{\mathcal{N}}$, $Q_{\mathcal{N}}$, and $R_{\mathcal{N}}$ can arise from, e.g., pump-induced modification of the electron and phonon occupations in the sample. Importantly, the pump-induced nonspin signal variations $\Delta P_{\mathcal{N}}$, $\Delta Q_{\mathcal{N}}$, and $\Delta R_{\mathcal{N}}$ cannot be separated from their spin counterparts $\Delta P_{\mathcal{S}}$, $\Delta Q_{\mathcal{S}}$, and $\Delta R_{\mathcal{S}}$ based on symmetry arguments. For example, $\Delta P_{\mathcal{N}} = \Delta P - \Delta P_{\mathcal{S}}$ has the same dependence on the pump- and probe-field polarization and sample azimuth as $\Delta P_{\mathcal{S}}$. Therefore, more sample-specific arguments need to be used to exclude sizeable nonspin contributions. For bare Mn_2Au, it was shown that the nonspin contributions are not dominant in $\langle Q\rangle$ [14].

Equation (5) suggests the following strategy to extract $\langle P\rangle$, $\langle Q\rangle$ and $\langle R\rangle$: We measure the signal S for at least three (typically four or eight) probe angles φ_{pr}, e.g., 0°, 45° and 90°. By

Fourier-transforming these data with respect to φ_{pr}, we can straightforwardly obtain $\langle P\rangle$, $\langle Q\rangle$, and $\langle R\rangle$ (Appendix B 1).

2. Non-normal probe incidence

To dedicatedly interrogate the magnetization of layer FM, we choose an angle of incidence of 30° for the probe beam. Importantly, in this case, the signal contributions linear in the order parameters can only arise from the local magnetization $\boldsymbol{M}$ because contributions linear in the Néel vector $\boldsymbol{L}$ are symmetry-forbidden in Mn_2Au (Appendix A 4 and Table IV).

Therefore, the relevant linear signal scales with $\langle \boldsymbol{M}\cdot\boldsymbol{u}_{pr}\rangle$, where $\boldsymbol{u}_{pr}$ is the unit vector along the probe propagation. We note that magnetization $\boldsymbol{M}$ can occur in layer FM, but also in the substrate ($\propto \boldsymbol{B}_{ext}$) and in layer AFM.

III. RESULTS

In the following, we first magneto-optically characterize the sample versus quasistatic variation of $\boldsymbol{B}_{ext}$. Next, we conduct THz-pump optical-probe measurements, which permit calibration of the magneto-optic signals with respect to $\boldsymbol{L}$ and $\boldsymbol{M}$. Finally, we use the obtained information to determine the volume fractions of the 0°, 90°, 180° and 270° domains in Mn_2Au.

A. Quasistatic variation of $\boldsymbol{B}_{ext}$

To characterize the static magnetic properties of the sample, we quasistatically vary the direction and amplitude of the applied in-plane magnetic field $\boldsymbol{B}_{ext}$ and simultaneously measure the probe signal S_0. In this context, quasistatic means timescales much slower than the expected spin dynamics with relaxation times below 10 ps [14].

We assume that variation of $\boldsymbol{B}_{ext}$ does not change the nonspin signals $P_{\mathcal{N}}$, $Q_{\mathcal{N}}$, $R_{\mathcal{N}}$. Therefore, any signal variation reports on changes in $P_{\mathcal{S}}$, $Q_{\mathcal{S}}$, $R_{\mathcal{S}}$ and, thus, in the magnetic order parameters of the sample stack according to Table I.

1. Variation of $\boldsymbol{B}_{ext}$ direction

In this section, we study how the magnetic order of the AFM|FM stack responds when the direction of $\boldsymbol{B}_{ext}$ is rotated within the easy plane of the antiferromagnet [Eq. (2)]. Accordingly, we measure the probe rotation S_0 versus the azimuthal angle $\varphi_{\boldsymbol{B}_{ext}}$ of $\boldsymbol{B}_{ext}$ with $B_{ext0} = 0.35$ T for four linear probe polarizations (Sec. II A and Fig. S2 [17]). By means of Eq. (5) and Appendix B 1, we obtain the signal contributions $\langle P_0\rangle$, $\langle Q_0\rangle$ and $\langle R_0\rangle$, which are displayed in Fig. 2(a).

The major signal variation versus $\varphi_{\boldsymbol{B}_{ext}}$ arises from component $\langle R_0\rangle$ of Eq. (5) [Fig. 2(a)]. A smaller contribution by $\langle Q_0\rangle$ is due potentially to a rotational offset of $\approx 6°$ between the probe-polarization plane and the sample's easy axis, which projects a small part of the dominant $\langle R_0\rangle$ part onto $\langle Q_0\rangle$. Finally, component $\langle P_0\rangle$ exhibits a minor dependence on $\varphi_{\boldsymbol{B}_{ext}}$ [Fig. 2(a)].

To understand the measured $\langle R_0\rangle$ versus $\varphi_{\boldsymbol{B}_{ext}}$, we first note that $\langle R_0\rangle$ equals the weighted spatial integral over $L^2_{\parallel 0}\cos(2\varphi_{\boldsymbol{L}})$ and $M^2_{\parallel 0}\cos(2\varphi_{\boldsymbol{M}})$ (Table I). As Mn_2Au is an easy-plane antiferromagnet [21], we assume that $L^2_{\parallel 0} \approx L_0^2$. Consequently, $\langle R_0\rangle$ versus $\varphi_{\boldsymbol{B}_{ext}}$ should vary symmetrically around zero. This property allows us to fix the unknown offset of the measured $\langle R_0\rangle$ vs $\varphi_{\boldsymbol{B}_{ext}}$, as already done in Fig. 2(a).

Importantly, as the signal $\langle R_0\rangle$ is obtained from the transmitted probe beam and involves a z integration (Appendix A 3), we expect it to increase approximately linearly with the thickness of the magnetic layers. Interestingly, Fig. 2(b) shows that $\langle R_0\rangle$ scales with the thickness of the Mn_2Au layer, but not that of the Py. Therefore, the measured $\langle R_0\rangle$ in Fig. 2(a) predominantly stems from Mn_2Au. Further, the signal vanishes when Mn_2Au and Py are separated by a thin layer of SiN_x and are, therefore, no longer exchange-coupled [Fig. 2(b)]. Because Mn_2Au is a collinear antiferromagnet, we can assume that $\boldsymbol{M}^{AFM} \approx 0$. Therefore, $\langle R_0\rangle$ can consistently be ascribed to the Néel vector of the Mn_2Au (Table I) and approximated as

$$\langle R_0\rangle = r_{\boldsymbol{L}} L_0^2 \langle\cos(2\varphi_{\boldsymbol{L}})\rangle, \tag{6}$$

where the sensitivity $r_{\boldsymbol{L}}$ is assumed to be homogeneous over the probed AFM volume.

The dependence of $\langle R_0\rangle$ on $\varphi_{\boldsymbol{B}_{ext}}$ indicates the following points. First, in the exchange-coupled samples, $\boldsymbol{M}^{FM}$ and $\boldsymbol{L}$ can be jointly set along any of the four easy axes by the external field, as indicated by the schematic in Fig. 2(a). Second, the signal changes abruptly between the saturated states at $\varphi_{\boldsymbol{B}_{ext}} \approx 0°$, 90°, 180° and 270°, virtually within the experimental step size of 15°. Thus individual regions of the probed volume reorient at approximately the same field angle $\varphi_{\boldsymbol{B}_{ext}}$, indicating that the spatial variation of the anisotropy is small. Third, the scaling of $\langle R_0\rangle$ with the thickness of the Mn_2Au thickness [Fig. 2(b)] indicates that $\boldsymbol{L}$ is controlled throughout the entire film, and not only in the interfacial layers adjacent to Py.

Note that, according to Eq. (6), saturation of $\langle R_0\rangle$ for $\boldsymbol{B}_{ext}$ along $\boldsymbol{u}_x$ or $\boldsymbol{u}_y$ implies, respectively, $\langle\cos(2\varphi_{\boldsymbol{L}})\rangle|_{sat} = \pm 1$ and, thus, signals of $\pm r_{\boldsymbol{L}} L_0^2$. The signals for opposite directions of $\boldsymbol{L}$ are always equal. From Fig. 2(a) and $\varphi_{\boldsymbol{B}_{ext}} = \varphi_{\boldsymbol{L}} = 0°$, we infer

$$\langle R_0\rangle|_{sat} = r_{\boldsymbol{L}} L_0^2 \approx 2.2 \text{ mrad} \tag{7}$$

for the probe rotation and also the ellipticity in magnetic saturation (sat). We, thus, obtain the first magneto-optic coefficient for the studied thin film, which is consistent with previous reflection-configuration studies on prealigned Mn_2Au films [22]. Its value can also be found in Table III and is comparable to the linear longitudinal magneto-optic-Kerr-effect signal, i.e., MCB, in Fe [19]. It exceeds the quadratic magneto-optic Kerr response, i.e., MLB, of ferromagnetic Py [23] and Fe [24] thin films by about one order of magnitude.

2. Variation of $\boldsymbol{B}_{ext}$ amplitude

Next, we study how the magnetic order of the AFM|FM stack reverses when the external magnetic field $\boldsymbol{B}_{ext}$ is reversed. To this end, we harmonically vary its amplitude B_{ext} along $\boldsymbol{u}_x$ [Eq. (2)] from $B_{ext}(0) = -B_{ext0}$ to $B_{ext}(T) = +B_{ext0} = 0.19$ T and back (Fig. 3 and Sec. II B 2). To obtain a high signal-to-noise ratio, one cycle is swept within the period $2T = 2$ ms and repeated over 10 runs.

Non-normal probe incidence. We start with probing under an angle of incidence of 30° and with a p-polarized probe.

This choice makes our probe sensitive to the magnetization $\langle \boldsymbol{M} \cdot \boldsymbol{u}_{\mathrm{pr}} \rangle$ along the probe propagation direction $\boldsymbol{u}_{\mathrm{pr}}$ through magneto-optic effects linear in the order parameters (Sec. II C 2 and Appendix A). The p polarization makes it insensitive to variations of $\boldsymbol{M}$ and $\boldsymbol{L}$ along $\boldsymbol{u}_x$ and $\boldsymbol{u}_y$ with respect to magneto-optic effects quadratic in the order parameters.

Figure 3(a) shows the resulting ellipticity signal versus time t, with (S_0) and without (S_0') the contribution $\propto \boldsymbol{B}_{\mathrm{ext}}$ of the substrate (see Fig. S3 [17]). The signal cannot arise from $\mathrm{Mn_2Au}$ because $\boldsymbol{M}^{\mathrm{AFM}} = 0$ in AFM in equilibrium, and because $\boldsymbol{L}$-related signals from $\mathrm{Mn_2Au}$ are exclusively even in $\boldsymbol{L}$, as dictated by symmetry (Appendix A). Therefore, the signal arises from Py. As the signal is predominantly odd in $\boldsymbol{B}_{\mathrm{ext}}$, it must be odd in the Py magnetization also and, thus, linear in $\boldsymbol{M}^{\mathrm{FM}}$ to lowest order. Consequently, we can safely attribute the signal in Fig. 3(a) to the Py magnetization $\langle \boldsymbol{M}^{\mathrm{FM}} \cdot \boldsymbol{u}_{\mathrm{pr}} \rangle \propto \langle M_x^{\mathrm{FM}} \rangle$.

We can separate S_0' into its contributions odd and even in $\boldsymbol{B}_{\mathrm{ext}}$ by

$$S_0'^{\pm} = \frac{S_0'(+\boldsymbol{B}_{\mathrm{ext}}) \pm S_0'(-\boldsymbol{B}_{\mathrm{ext}})}{2}. \tag{8}$$

When plotted versus B_{ext}, the signal S_0' attains the shape of a squarelike hysteresis loop [Fig. 3(b),] as expected for the magnetization of a ferromagnetic thin film with easy-plane magnetic anisotropy. The value of the coercive field B_{c} amounts to ≈ 0.08 T and is consistent with previous magnetometry and ferromagnetic-resonance studies [15,16]. Importantly, the B_{c} value is much higher than for bare Py thin films where $B_{\mathrm{c}} \sim 1$ mT [25]. This observation implies a strong exchange coupling between Py and $\mathrm{Mn_2Au}$ and a saturated magnetic state for the peak magnetic field in our experiment.

Normal probe incidence. From now on, we proceed with probing under standard normal probe incidence (Sec. II C 2). Figure 3(b) shows the extracted magneto-optic signal contributions $\langle P_0 \rangle$, $\langle Q_0 \rangle$, and $\langle R_0 \rangle$ versus time t along with $B_{\mathrm{ext}}(t)$. First, as with the data in Fig. 2(a) and Eq. (6), $\langle R_0 \rangle$ reports on the weighted spatial integral $L_0^2 \langle \cos(2\varphi_L) \rangle$, which equals L_0^2 in saturation. Consequently, to fix the unknown signal offset of $\langle R_0 \rangle$ versus B_{ext}, we assume that, at the maximum field of B_{ext0}, the signal saturates and, thus, equals the peak signals in Fig. 2(a) where $B_{\mathrm{ext0}} = 0.35$ T.

Second, the signal minimum of $\langle R_0 \rangle \approx 0$ at $B_{\mathrm{ext}} \approx 0.08$ T implies $\langle \cos(2\varphi_L) \rangle \propto \langle L_x^2 - L_y^2 \rangle \approx 0$ and, thus, $\langle L_x^2 \rangle \approx \langle L_y^2 \rangle$ [Eq. (6) and Table I]. In other words, the volume fractions of $\boldsymbol{u}_x$- and $\boldsymbol{u}_y$-type domains are approximately equal. At the same field B_{ext}, $\langle Q_0 \rangle \propto \langle L_x L_y \rangle$ is relatively small, indicating that $\boldsymbol{L}$ does not reverse by uniform rotation in the probed volume, but by nucleation and growth of laterally extended domains [26]. The minimum of $\langle R_0 \rangle$ can only be explained by nucleation of $\pm \boldsymbol{u}_y$ domains, since a reversal involving only $\pm \boldsymbol{u}_x$ domains would leave the signal constant as $\boldsymbol{B}_{\mathrm{ext}}$ changes. Finally, the signal minimum of $\langle R_0 \rangle \approx 0$ implies a coercive field of $B_{\mathrm{c}} \approx 0.1$ T, consistent with our complementary measurements of $\langle M_x^{\mathrm{FM}} \rangle$ [Fig. 3(a)].

To summarize, our results of Figs. 2 and 3 indicate that the Néel vector $\boldsymbol{L}$ of layer AFM reverses upon passing the coercive field of the stack AFM|FM. This notion is illustrated by the schematic at the bottom of Fig. 3(b). We note that the volume of domains with $\boldsymbol{L}_0 \upuparrows +\boldsymbol{u}_x$ and $\boldsymbol{L}_0 \upuparrows -\boldsymbol{u}_x$ cannot be obtained from the measurements we have presented so far. We will show in Sec. III C that the precise domain volume fractions can be obtained from the pump-probe signals.

B. Pump-probe signals

Following a magneto-optic characterization of our $\mathrm{Mn_2Au}$|Py sample as a function of a quasistatic external magnetic field $\boldsymbol{B}_{\mathrm{ext}}$ (Figs. 2 and 3), we now excite it with a normally incident THz electromagnetic field $F = (\boldsymbol{E}, \boldsymbol{B})$ (Fig. 1). This pump pulse induces a variation of the probe signal by $\Delta S(t) = S(t) - S_0(t)$, which depends on the delay $\tau = t - t_{\mathrm{pu}}$ between pump and probe.

To separate signal contributions to $\Delta S(t)$ linear and quadratic in F, we use pump fields $\pm F$ of opposite polarity (Sec. II B 1). To better separate spin- and non-spin-related signals, we further reverse the polarity of the external magnetic field $\boldsymbol{B}_{\mathrm{ext}} = B_{\mathrm{ext}} \boldsymbol{u}_x$ analogous to Fig. 3(b), thereby switching B_{ext} between ± 0.19 T at every other pump pulse.

1. Expected signal contributions and temporal responses

According to Eq. (5), $\Delta S(t)$ arises from pump-induced changes $\langle \Delta P \rangle$, $\langle \Delta Q \rangle$ and $\langle \Delta R \rangle$. In contrast to the quasistatic case, the signals may not only have contributions $\Delta P_{\mathcal{S}}$, $\Delta Q_{\mathcal{S}}$ and $\Delta R_{\mathcal{S}}$ related exclusively to spin dynamics but also contributions $\Delta P_{\mathcal{N}}$, $\Delta Q_{\mathcal{N}}$ and $\Delta R_{\mathcal{N}}$. The latter report on changes in nonspin degrees of freedom, which we discuss separately in the following.

True pump-induced spin dynamics. We start with mechanisms of true pump-induced spin dynamics, such as spin torques and ultrafast demagnetization, and the signal they result in.

Linear responses. To facilitate further discussion, we first focus on the most common types of spin dynamics in linear response to a THz electromagnetic field. Formally, the linear response of the component Y of a magnetic order parameter to a component X of the driving THz field $F = (\boldsymbol{E}, \boldsymbol{B})$ can be written as

$$\Delta Y(t) = (H_{\Delta Y \leftarrow X} * X)(t) = \int \mathrm{d}t' H_{\Delta Y \leftarrow X}(t - t') X(t'). \tag{9}$$

Here, $H_{\Delta Y \leftarrow X}(t)$ is the response $\Delta Y(t)$ to an impulsive driving field component $X(t') = \delta(t')$ at time $t' = 0$. Table II and Fig. 4 summarize possible X, ΔY and $H_{\Delta Y \leftarrow X}$ mathematically and graphically, respectively. Prominent examples of linear responses are spin torques on the magnetic order in the FM and AFM.

First, the fieldlike Zeeman torque $\propto \boldsymbol{M}^{\mathrm{FM}} \times \boldsymbol{B}$ by the magnetic field $\boldsymbol{B}$ of the THz pulse perturbs the magnetization $\boldsymbol{M}^{\mathrm{FM}}$ of the FM of Py [19,27,28]. The resulting transient out-of-plane magnetization component ΔM_z^{FM} may be detected through term $\langle \Delta P \rangle$ [Eq. (5) and Table I]. The subsequent precession in the gigahertz range is so slow that $H_{\Delta Y \leftarrow X}$ is a step function on the picosecond timescale (Table II and Fig. 4).

The Zeeman torque may also excite dynamics in the AFM of $\mathrm{Mn_2Au}$ [29]. In our sample geometry, we expect an out-of-plane contribution ΔL_z as well as an in-plane magnetization ΔM_y [14]. From Raman-scattering experiments [30] and

TABLE II. Possible spin dynamics due to linear response to a terahertz pump field $F = (\boldsymbol{E}, \boldsymbol{B})$. Here, $\Theta(t)$ denotes the Heaviside step function, and $\boldsymbol{M}_0^{\mathrm{FM}} \parallel \boldsymbol{L}_0 \parallel \boldsymbol{u}_x$ is assumed. ZT and NSOT stands for, respectively, fieldlike Zeeman torque and fieldlike Néel spin-orbit torque.

Magnetic order parameter ΔY	Sensitive signal component	Driving field	Mechanism	Response function $H_{\Delta Y \leftarrow X}$ is proportional to	Resonance frequency $\boldsymbol{\Omega}/2\pi$
ΔM_z^{FM}	$\langle \Delta P \rangle$	B_y	ZT	$\cos(\Omega t)\mathrm{e}^{-\Gamma t}\Theta(t)$	~15 GHz [15]
ΔL_z	–	B_y	ZT	$H_{\Delta L_z \leftarrow B_y}(t) = \cos(\Omega t)\mathrm{e}^{-\Gamma t}\Theta(t)$	~3 THz [30,31]
$\Delta M_y^{\mathrm{AFM}}$	$\langle \Delta R \rangle$ (small)	B_y	ZT	$\partial_t H_{\Delta L_z \leftarrow B_y}$	~3 THz
$\Delta \varphi_{\boldsymbol{L}}$	$\langle \Delta Q \rangle$, $\langle \Delta R \rangle$	E_x	NSOT	$H_{\Delta \varphi_{\boldsymbol{L}} \leftarrow E_x}(t) = (1/\Omega)\sin(\Omega t)\mathrm{e}^{-\Gamma t}\Theta(t)$	~0.5 THz [14]
$\Delta M_z^{\mathrm{AFM}}$	$\langle \Delta P \rangle$	E_x	NSOT	$\partial_t H_{\Delta \varphi_{\boldsymbol{L}} \leftarrow E_x}$	~0.5 THz

theory [31], a resonance frequency of roughly 3-4 THz is estimated. However, the signal contribution from this mode can be neglected in our geometry, as we lack sensitivity to ΔL_z, and the net ΔM_y is expected to be very small [14].

Second, in Mn_2Au, fieldlike Néel spin-orbit torque (NSOT) by the THz electric field $\boldsymbol{E}$ leads to in-plane rotation of $\boldsymbol{L}$ by an angle $\Delta\varphi_{\boldsymbol{L}}$ and to an out-of-plane magnetization $\Delta M_z^{\mathrm{AFM}}$ [14]. The $\Delta M_z^{\mathrm{AFM}}$ can straightforwardly be explained by the macrospin σ-model for antiferromagnets [32–34]. It implies that the dynamic magnetization $\Delta \boldsymbol{M}^{\mathrm{AFM}}$ of an antiferromagnet with $|\Delta \boldsymbol{M}^{\mathrm{AFM}}| \ll |\boldsymbol{L}|$ follows the Néel vector $\boldsymbol{L}$ through

$$\Delta \boldsymbol{M}^{\mathrm{AFM}} \approx \frac{1}{\gamma B_{\mathrm{ex}} L_0} \boldsymbol{L} \times \partial_t \boldsymbol{L}, \tag{10}$$

where γ is the gyromagnetic ratio and B_{ex} is the exchange field. In Mn_2Au, the in-plane rotation of the Néel vector by $\Delta\varphi_{\boldsymbol{L}}$ is resonant and related to a magnon [Fig. 1(c)] [14] whose oscillatory motion is summarized in Table II and Fig. 4. If the $\boldsymbol{L}$ motion is dominated by the in-plane oscillation $\Delta\varphi_{\boldsymbol{L}}$, Eq. (10) results in $\Delta M_z^{\mathrm{AFM}} \propto L_0^2 \partial_t \Delta\varphi_{\boldsymbol{L}}$, and the response functions of $\Delta\varphi_{\boldsymbol{L}}$ and $\Delta M_z^{\mathrm{AFM}}$ are related by a time derivative as well (Table II and Fig. 4).

Quadratic responses. While Zeeman torque and NSOT can already induce changes in $\boldsymbol{M}$ and $\boldsymbol{L}$ to linear order in the driving field F, there can also be changes that scale with the square of F to lowest order. An important example is ultrafast quenching of magnetic order by a THz electric field $\boldsymbol{E}$ that increases the energy of electrons $\propto \boldsymbol{E}^2$ [35]. In our probing geometry and for the AFM, a reduction of $|\boldsymbol{L}|$ could be probed by the spin-related signal contribution $\Delta R_{\mathcal{S}}^{+} \propto \Delta(L_x^2) \approx 2L_{0x}\Delta L_x$ (Table I).

Nonspin contributions. The signal contributions $\Delta S_{\mathcal{N}}$ that, at least partially, report on the dynamics of nonspin degrees of freedom $\mathcal{N}$ can be classified in (i) symmetry-conserving and (ii) symmetry-breaking variations of $\mathcal{N}$.

A possible microscopic scenario of (i) is an isotropic increase of the energy of electrons or phonons in AFM or FM. It scales with the energy density $\propto \boldsymbol{E}^2$ of the driving THz field to lowest order. Because the sample symmetry is not lowered in this process, the resulting signal changes have the same structure as the $P_{\mathcal{S}}$, $Q_{\mathcal{S}}$ and $R_{\mathcal{S}}$ in Table I. However, as the spin

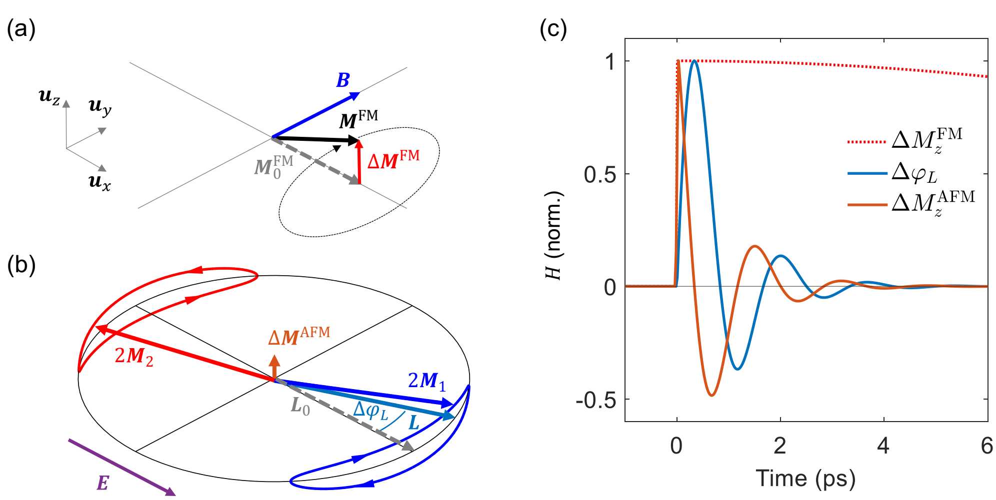

FIG. 4. Expected spin dynamics and response functions linear in the driving THz field $F = (\boldsymbol{E}, \boldsymbol{B})$. (a) Layer FM has magnetization $\boldsymbol{M}_0^{\mathrm{FM}}$ (gray dashed arrow) before arrival of F. Fieldlike Zeeman torque (ZT) of the THz magnetic field $\boldsymbol{B}$ leads to an out-of-plane dynamic magnetization change $\Delta \boldsymbol{M}^{\mathrm{FM}} \parallel \boldsymbol{u}_z$ and a subsequent precession of $\boldsymbol{M}^{\mathrm{FM}} = \boldsymbol{M}_0^{\mathrm{FM}} + \Delta \boldsymbol{M}^{\mathrm{FM}}$. (b) Spin dynamics in layer AFM is driven through fieldlike Néel spin-orbit torque (NSOT) of the THz electric field $\boldsymbol{E}$. NSOT leads to an out-of-plane magnetization $\Delta \boldsymbol{M}^{\mathrm{AFM}}$ and in-plane deflection of the Néel vector $\boldsymbol{L}$ by an angle $\Delta\varphi_L$. (c) Resulting impulse-response functions $H_{\Delta Y \leftarrow X}$ for various response observables ΔY [Eq. (9) and Table II]. In the FM, magnetization ΔM_z^{FM} is induced by ZT (red-dashed line). In AFM, NSOT causes an in-plane deflection $\Delta\varphi_L$ of the Néel vector (blue line) and an out-of-plane magnetization $\Delta M_z^{\mathrm{AFM}}$ (orange line).

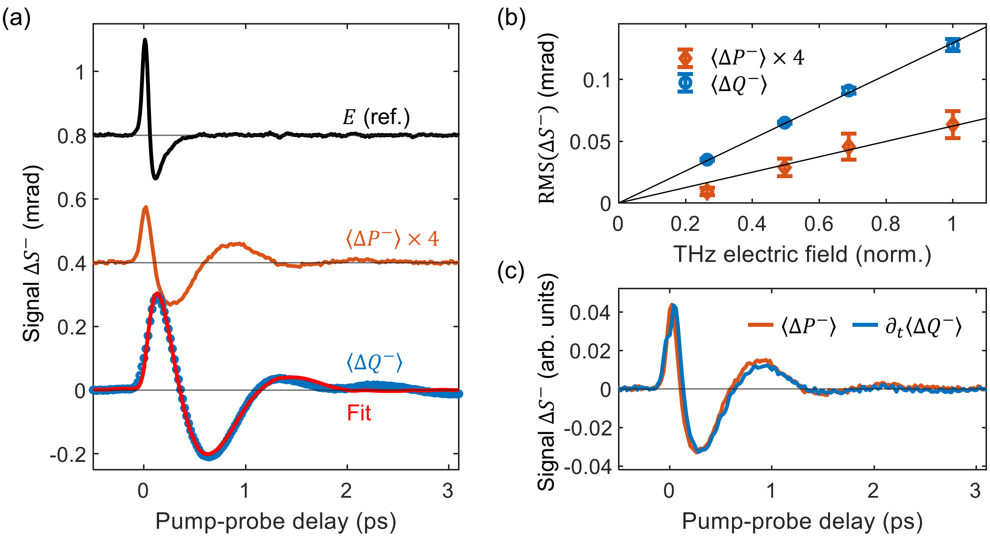

FIG. 5. Pump-probe signal components odd in both THz pump field F and external magnetic field $\boldsymbol{B}_{\text{ext}}$. (a) Ellipticity-signal components $\langle \Delta P^- \rangle$ (orange line) and $\langle \Delta Q^- \rangle$ (blue circles), along with the THz pump electric field (black). Signals are extracted according to Eq. (5) from eight linear polarization angles (Appendixes A 3 and B 1). Raw data are shown in Fig. S5 [17]. Signals are scaled and vertically offset for clarity. The red line shows a fit to signal $\langle \Delta Q^- \rangle$ according to the response function in Table II. (b) RMS of $\langle \Delta P^- \rangle$ and $\langle \Delta Q^- \rangle$ (Fig. S9 [17]) vs pump electric-field strength. The black lines are linear fits. (c) Signal $\langle \Delta P^- \rangle$ (orange line) and scaled numerical derivative $\partial_t \langle \Delta Q^- \rangle$ of signal $\langle \Delta Q^- \rangle$ (blue line).

degrees of freedom remain unchanged, $\mathcal{S} = \mathcal{S}_0$, the signal is mediated by variations of magneto-optic coefficients, such as $r_{\boldsymbol{L}}$ [35–37]. Therefore, the signal ΔR has a non-spin-related component of the form $\Delta R_{\mathcal{N}} = L_{\parallel 0}^2 \cos(2\varphi_{\boldsymbol{L}_0}) \Delta r_{\boldsymbol{L}}$, which cannot be distinguished from pure spin dynamics using symmetry arguments.

Even more challenging, effects quadratic in $\boldsymbol{E}$ are of even order in $\boldsymbol{L}_0$ and can, therefore, not be separated from contributions of nonmagnetic sample parts by reversal of $\boldsymbol{L}_0$. An example is the THz Kerr effect [38,39] in the substrate of our sample.

A possible microscopic mechanism leading to (ii) is a $\boldsymbol{E}$-induced shift of the Fermi sphere of AFM or FM. The shift scales with $\boldsymbol{E}$ to lowest order, is accompanied by a net electron current and transiently lowers the sample symmetry. Phenomenologically, it is most suitably described in explicit terms of the driving field [14]. For example, for ΔQ, the respective contribution can be written as $\Delta Q_{\mathcal{N}} \propto L_{0x} E_x - L_{0y} E_y$. Therefore, even though this specific $\Delta Q_{\mathcal{N}}$ reverses as $\boldsymbol{L}_0$ is reversed, it cannot be distinguished from its truly spin-related counterpart $\Delta Q_{\mathcal{S}}$ based on symmetry properties.

Therefore, in the following, we will make use of more specific arguments for the spin-dominant nature of the measured signals.

2. Raw-signal analysis

Typical pump-probe signals $\Delta S(t)$ are shown in Figs. S5 and S6 [17] for various probe-polarization angles φ_{pr} [Fig. 1(b)]. Both rotation and ellipticity signals are acquired, as noted in the text whenever applicable. We extract the signal contributions $\langle \Delta P \rangle$, $\langle \Delta Q \rangle$, and $\langle \Delta R \rangle$ of Eq. (5) based on their probe-polarization dependence, as detailed in Sec. II C and Appendix B 1. All contributions are shown in Fig. S7 [17].

At first glance, signals that stem exclusively from spin dynamics are expected to exhibit the same temporal dynamics in both rotation (rot) and ellipticity (ell), e.g., $\langle \Delta P(\tau) \rangle|_{\text{rot}} \propto \langle \Delta P(\tau) \rangle|_{\text{ell}}$ [35–37]. Note, however, that different contributions, such as Zeeman torque and NSOT, may contribute with different relative weight to $\langle \Delta P(\tau) \rangle|_{\text{rot}}$ and $\langle \Delta P(\tau) \rangle|_{\text{ell}}$ and, thus, cause different dynamics of these two observables. Consequently, in the following, we will first focus on signals that can be well explained by a single signal contribution from Table I.

We start with signals odd in both the driving field F and the quasistatic external magnetic $\boldsymbol{B}_{\text{ext}}$ (Fig. 5) and subsequently consider signals even in both F and $\boldsymbol{B}_{\text{ext}}$ (Fig. 6). In other words, odd and even signals $\Delta S^{\pm}$ are given by

$$\Delta S^{\pm} = \frac{\Delta S(+F, +\boldsymbol{B}_{\text{ext}}) \pm \Delta S(-F, +\boldsymbol{B}_{\text{ext}}) \pm \Delta S(+F, -\boldsymbol{B}_{\text{ext}}) + \Delta S(-F, -\boldsymbol{B}_{\text{ext}})}{4}, \tag{11}$$

and, in an analogous manner, their odd and even components $\langle \Delta P^{\pm} \rangle$, $\langle \Delta Q^{\pm} \rangle$ and $\langle \Delta R^{\pm} \rangle$.

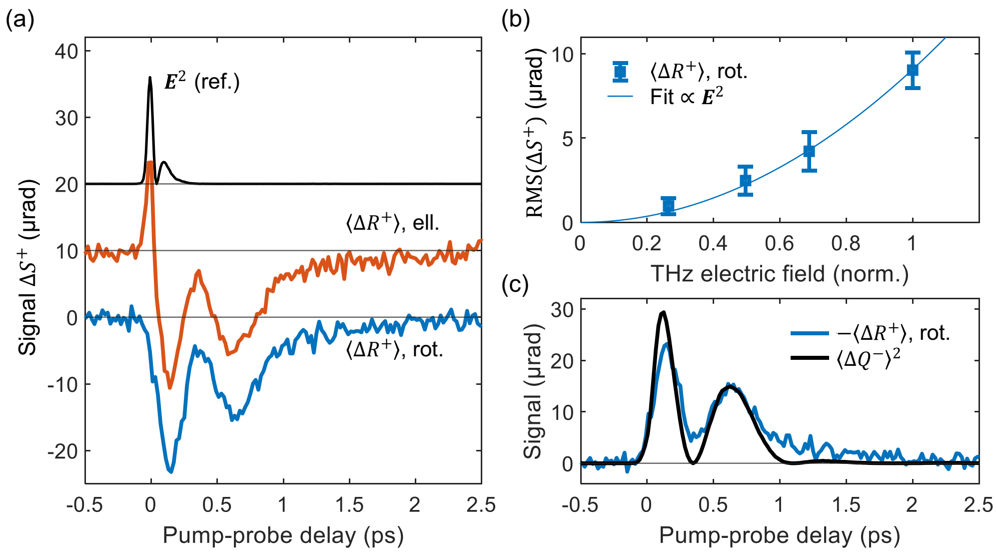

FIG. 6. Pump-probe signal components even in F and $\boldsymbol{B}_{\text{ext}}$. (a) Pump-probe signal component $\langle\Delta R^+\rangle$ even in both THz pump field F and external magnetic field $\boldsymbol{B}_{\text{ext}}$. The signal is extracted according to Eq. (5) from eight linear polarization angles (Figs. S5 and S6 [17]) and measured as probe ellipticity (orange line) and rotation (blue line). The black solid line shows the pump energy density $\propto \boldsymbol{E}^2(\tau)$. (b) RMS of the rotation signal (Fig. S10 [17]) vs pump electric-field strength along with quadratic fit. (c) Signal $-\langle\Delta R^+\rangle$ (rotation, blue line) and scaled signal $\langle\Delta Q^-\rangle^2$ (black line).

3. Odd signals and interpretation

In this section, we focus on signals that are odd in F and $\boldsymbol{B}_{\text{ext}}$, and, thus, also odd in $\boldsymbol{M}_0^{\text{FM}}$ and $\boldsymbol{L}_0$. These signals are expected to contain the linear-response-type dynamics discussed in Sec. III B 1.

As seen in Fig. S7 [17], the dominant components of the probe ellipticity signal ΔS^- odd in F and $\boldsymbol{B}_{\text{ext}}$ are $\langle\Delta P^-\rangle$ and $\langle\Delta Q^-\rangle$. They are shown in Fig. 5(a) along with the measured driving electric field. Figure 5(b) confirms that the probe ellipticity signal ΔS^- odd in F and $\boldsymbol{B}_{\text{ext}}$ scales linearly with the THz field F. In other words, the signals in Fig. 5(a) characterize the linear-response regime. Once the driving THz field has decayed, both $\langle\Delta P^-\rangle$ and $\langle\Delta Q^-\rangle$ feature an oscillatory pattern [Fig. 5(a)], which is reminiscent of the expected response functions shown in Table II and Fig. 4.

However, for the probe rotation signals, we observe more complex dynamics with additional contributions, which can be attributed to further processes, as we discuss below (Figs. S7 and S8 [17]). Here, we focus on the ellipticity signals.

According to Tables I and II, the MCB component $\langle\Delta P\rangle$ contains a term due to the dynamic out-of-plane magnetization ΔM_z, while the MLB component $\langle\Delta Q\rangle$ contains terms due to the in-plane Néel vector through $2\Delta(L_xL_y) \approx 2L_{\parallel 0}^2\Delta\varphi_{\boldsymbol{L}}$ and the in-plane magnetization through $2\Delta(M_xM_y)$. The occurrence of dynamic variations of $\varphi_{\boldsymbol{L}}$ and M_z^{AFM} linear in F and $\boldsymbol{B}_{\text{ext}}$ is consistent with the NSOT-driven homogeneous in-plane magnon of Mn_2Au [14]. Accordingly, we fit the signal as $\Delta\varphi_{\boldsymbol{L}} \propto H_{\Delta\varphi_{\boldsymbol{L}}\leftarrow E_x} * E_x$ with the impulse response function $H_{\Delta\varphi_{\boldsymbol{L}}\leftarrow E_x}$ (Table II). We obtain a frequency of $\Omega/2\pi = 0.6$ THz and damping rate $\Gamma = 2.3\ \text{ps}^{-1}$, which agree with previous results for a bare Mn_2Au film [14]. The excellent agreement between data and fit supports the assignment

$$\langle\Delta Q^-\rangle = 2q_{\boldsymbol{L}}L_0^2\langle\Delta\varphi_{\boldsymbol{L}}\rangle, \tag{12}$$

where we used $L_{\parallel 0} = L_0$. Figure 5(c) further reveals that the calculated time derivative $\partial_t\Delta\langle Q^-\rangle$ largely agrees with $\Delta\langle P^-\rangle$. This behavior is expected from the σ-model [Eq. (10)] and indicates that

$$\langle\Delta P^-\rangle = p_{\boldsymbol{M}}\langle\Delta M_z^{\text{AFM}}\rangle. \tag{13}$$

As the magnetization change $\Delta\boldsymbol{M}^{\text{FM}}$ of FM is expected to follow a different response function (Table II), we conclude that it is not efficiently probed in the ellipticity signal.

We note that the signal assignments by Eqs. (12) and (13) for Mn_2Au|Py are fully consistent with our previous findings on prealigned Mn_2Au films [14]. In these samples, the smaller contribution $\propto \Delta M_z^{\text{AFM}}$ could not be detected in $\langle\Delta P^-\rangle$, presumably due to the smaller signal-to-noise ratio.

The odd-in-F-and-$\boldsymbol{B}_{\text{ext}}$ signal $\langle\Delta Q^-\rangle$ characterizes the temporal dynamics of $\langle\Delta\varphi_{\boldsymbol{L}}\rangle$ well [Eq. (12)]. However, it cannot determine the absolute magnitude of the deflection $\langle\Delta\varphi_{\boldsymbol{L}}\rangle$. A static calibration of the necessary magneto-optic coefficient $q_{\boldsymbol{L}}L_0^2$ as done in Sec. III A 1 for $r_{\boldsymbol{L}}L_0^2$, is not possible since the static signal $\langle Q_0\rangle$ vanishes. We, thus, look for an even pump-probe contribution $\langle\Delta R^+\rangle$ that could be calibrated by a nonvanishing $\langle R_0\rangle$.

4. Even signals

In this section, we consider whether the pump-probe signal contribution $\langle\Delta R^+\rangle$ reports on the dynamics of $\boldsymbol{L}$ and could, thus, be used to gain additional insights into the amplitude of the deflection of $\Delta\varphi_{\boldsymbol{L}}$. Consequently, we turn to the signal ΔS^+ even in F and $\boldsymbol{B}_{\text{ext}}$ [Eq. (11)]. As discussed in Secs. III B 1 and III B 2, ΔS^+ as well can have a variety of non-spin-related contributions $\Delta S_{\mathcal{N}}^+$. They are even more challenging to identify than in ΔS^- because, by definition, ΔS^- changes sign as, e.g., $\boldsymbol{L}_0$ is reversed, whereas ΔS^+ remains

TABLE III. Table of extracted magneto-optic coefficients. All coefficients are given for the layer AFM of Mn_2Au with a thickness of 50 nm and for the probe wavelength of 800 nm. The MCB component is given for $M_z^{\rm AFM} = L_0$.

Component	Type	Coefficient	Rotation (mrad)	Ellipticity (mrad)
P	MCB	$p_{\boldsymbol{M}} M_z^{\rm AFM}$	8	16
Q	MLB	$q_{\boldsymbol{L}} L_0^2$	0.3	1.8
R	MLB	$r_{\boldsymbol{L}} L_0^2$	2.2	2.2

unchanged. Therefore, ΔS^+ can have contributions that are completely unrelated to the $\boldsymbol{L}_0$ of the sample.

Figure 6(a) shows component $\langle \Delta R^+ \rangle$ for both rotation and ellipticity signals. Figure 6(b) confirms the signals of Fig. 6(a) scale with the square F^2 of the driving field, which is the lowest order even in F.

Note that the ellipticity- and rotation-type $\langle \Delta R^+ \rangle$ coincide once the instantaneous pump energy density $\propto \boldsymbol{E}^2(\tau)$ becomes negligible [$\tau > 0.2$ ps, Fig. 6(a)]. In the ellipticity signal, an additional sharp feature is present close to the overlap of pump and probe pulses ($\tau \approx 0$ ps), which we attribute to a spin-unrelated refractive-index change of the metallic film. Importantly, the otherwise identical dynamics of the ellipticity- and rotation-type $\langle \Delta R^+ \rangle$ suggests that both signals report on the same component of spin dynamics. An even signal $\Delta R_{\mathcal{N}}$ from the MgO substrate is possible, but would be box-shaped and extend over a much longer delay than 0.2 ps [39]. It can, thus, be discarded here.

According to Table I, the spin-related contribution to $\langle \Delta R^+ \rangle$ is a superposition of $\Delta \langle L_{0\parallel}^2 \cos(2\varphi_{\boldsymbol{L}}) \rangle$ and $\Delta \langle M_{0\parallel}^2 \cos(2\varphi_{\boldsymbol{M}}) \rangle$, i.e., a change in (i) the in-plane magnitudes ($L_{0\parallel}, M_{0\parallel}$) and/or (ii) rotation ($\varphi_{\boldsymbol{L}}, \varphi_{\boldsymbol{M}}$) of the order parameters $\boldsymbol{L}, \boldsymbol{M}$. Assuming scenario (ii) prevails, the signal would scale according to $\langle \Delta R^+ \rangle \propto \Delta \langle \cos(2\varphi_{\boldsymbol{L}}) \rangle \approx 2\langle (\Delta\varphi_{\boldsymbol{L}})^2 \rangle$ and, thus, obey

$$\langle \Delta R^+ \rangle = 2 r_{\boldsymbol{L}} L_0^2 \langle (\Delta\varphi_{\boldsymbol{L}})^2 \rangle. \tag{14}$$

In this case, Eqs. (12) and (14) imply that the signal $\langle \Delta R^+ \rangle$ would scale with the square of signal $\langle \Delta Q^- \rangle$. Indeed, the direct comparison of $\langle \Delta Q^- \rangle$ [Fig. 5(a)] and $\langle \Delta R^+ \rangle$ [Fig. 6(a)] in Fig. 6(c) confirms that, approximately, $\langle \Delta R^+(t) \rangle \propto \langle \Delta Q^-(t) \rangle^2$. This remarkable agreement indicates that scenario (i), i.e., ultrafast magnetic-order quenching by pump-induced heating of Mn_2Au and Py, makes a minor contribution to $\langle \Delta R^+ \rangle$.

Due to the square operation, the signal $\langle \Delta R^+(t) \rangle \propto [\Delta\varphi_{\boldsymbol{L}}(t)]^2$ displays ultrafast dynamics with twice the frequency of $\langle \Delta Q^-(t) \rangle \propto \Delta\varphi_{\boldsymbol{L}}(t)$. This feature is consistent with similar observations in the insulating antiferromagnet NiO [40].

We emphasize that the observed pump-induced changes in the Néel vector and signal $\langle \Delta Q^- \rangle$ scale linearly with the pump field F [Fig. 5(b)], whereas the quadratic scaling of $\langle \Delta R^+ \rangle$ [Fig. 6(b)] is just a consequence of the probe process [Table I, Eqs. (12) and (14)]. Thus, our findings indicate that we probe the in-plane rotation $\Delta\varphi_{\boldsymbol{L}}$ of the Néel vector of Mn_2Au through both $\langle \Delta Q^- \rangle$ and $\langle \Delta R^+ \rangle$ in a complementary manner.

5. Absolute deflection angle and magneto-optic coefficients

Our findings in Sec. III B 4 indicate that the even signal $\langle \Delta R^+ \rangle$ probes the in-plane $\boldsymbol{L}$ deflection, as summarized by Eq. (14). Remarkably, this observable has a measurable nonvanishing quasistatic analog $\langle R_0 \rangle$, which can be used to calibrate the pump-induced signal $\langle \Delta R^+ \rangle$ and, thus, the magnitude of the transient deflection angle $\Delta\varphi_{\boldsymbol{L}}$.

To carry out this calibration, we assume that the sample is in the magnetically saturated state and acknowledge that the probe spot is much smaller than the THz pump spot. Consequently, the Néel vector $\boldsymbol{L}_0$ and the pump electric field $\boldsymbol{E}$ are homogeneous over the probed sample volume, resulting in $\langle \cos(2\varphi_{\boldsymbol{L}}) \rangle = 1$ and, thus, $\langle R_0 \rangle = r_{\boldsymbol{L}} L_0^2$ for the quasistatic case, and $\langle (\Delta\varphi_{\boldsymbol{L}})^2 \rangle = (\Delta\varphi_{\boldsymbol{L}})^2$ and, thus, $\langle \Delta R^+ \rangle = -2 r_{\boldsymbol{L}} L_0^2 (\Delta\varphi_{\boldsymbol{L}})^2$ for the pump-probe signal. Therefore, we obtain the absolute $(\Delta\varphi_{\boldsymbol{L}})^2$ by taking

$$\left| \frac{\langle \Delta R^+ \rangle}{\langle R_0 \rangle} \right| \Bigg|_{\rm sat} = 2(\Delta\varphi_{\boldsymbol{L}})^2, \tag{15}$$

which determines the proportionality coefficient $\langle (\Delta\varphi_{\boldsymbol{L}})^2 \rangle / \langle \Delta R^+ \rangle$ of Eq. (14) in magnetic saturation (sat). Importantly, knowledge of $(\Delta\varphi_{\boldsymbol{L}})^2$ allows us to further calibrate the proportionality coefficient $\langle \Delta\varphi_{\boldsymbol{L}} \rangle / \langle \Delta Q^- \rangle$ of Eq. (12) by using

$$\sqrt{\langle \Delta Q^- \rangle^2 \left| \frac{\langle R_0 \rangle}{\langle \Delta R^+ \rangle} \right|} \Bigg|_{\rm sat} = \left| q_{\boldsymbol{L}} L_0^2 \right|. \tag{16}$$

Note that Eq. (12) is valid for all pump-probe delays, whereas Eqs. (14)–(16) are accurate for pump-probe delays $\tau > 0.3$ ps, i.e., after the pump pulse has decayed (Sec. III B 4). We obtain a peak deflection of $\Delta\varphi_{\boldsymbol{L}} = -5^\circ$ at $\tau = 0.13$ ps, and find that $|q_{\boldsymbol{L}} L_0^2|$ in the probe-pulse ellipticity amounts to 1.8 mrad. As shown in Fig. S8 [17], $q_{\boldsymbol{L}} L_0^2$ is about 6 times smaller in the probe-pulse rotation than the ellipticity. We emphasize that $q_{\boldsymbol{L}} L_0^2$ cannot be accessed in the static sample state, and its calibration always requires a dynamic process, e.g., the excitation of the in-plane magnon as done here.

With $\Delta\varphi_{\boldsymbol{L}}$ and Eq. (10), we further determine the relative transient magnetization in layer AFM through $\Delta M_z^{\rm AFM}/L_0 = \Delta\varphi_{\boldsymbol{L}}/\gamma B_{\rm ex}$. With $B_{\rm ex} = 1300$ T [21] and the gyromagnetic ratio $\gamma = 0.176\ {\rm T^{-1}\,ps^{-1}}$ of the electron, we find that $\Delta M_z^{\rm AFM}/L_0$ reaches a maximum value of 2.7×10^{-3}. It is interesting to use this value to estimate the maximum MCB signal change (Table I) due to a hypothetical spin-flip transition in AFM, where both spin sublattices finally align parallel to $\boldsymbol{u}_z$, i.e., $\Delta M_z^{\rm AFM}/L_0 = 1$. We obtain 16 mrad (probe-pulse ellipticity) and 8 mrad (probe-pulse rotation, Fig. S8 [17]). Thus the MCB signal due to $\Delta M_z^{\rm AFM} = L_0$ is about one order of magnitude larger than the maximum attainable MLB signal. However, in our pump-probe experiment, the induced MCB signals are smaller than the MLB signals due to the small AFM net magnetization.

Finally, by estimating the THz electric field strength inside layer AFM with the Tinkham formula [41] and an average conductivity of 8.8 ${\rm MS\,m^{-1}}$, we determine a torkance of 90 ${\rm cm^2\,A^{-1}\,s^{-1}}$ (Appendix B 5). We emphasize that this value is in good agreement with our previous estimate based on the onset of nonlinear magnon dynamics [14].

This subsection completes the characterization of the magneto-optical coefficients of layer AFM, which are summarized in Table III for both probe-polarization rotation and ellipticity. The observables $\langle \Delta Q^- \rangle$ [Eq. (12)], $\langle \Delta P^- \rangle$ [Eq. (13)] and $\langle \Delta R^+ \rangle$ [Eq. (14)] provide complementary information on the magnetic order parameters of AFM through the Néel-vector deflection $\Delta\varphi_L$ and the dynamic magnetization M_z^{AFM}. Their calibration is enabled by the magnetically saturated state [Eqs. (15) and (16)].

C. Revealing the domain distribution

So far, we have focused on the saturated, i.e., virtually uniform, magnetic state of the sample. In a nonsaturated state, we expect different magnitudes of the contributions $\langle \Delta Q^- \rangle$ [Eq. (12)] and $\langle \Delta R^+ \rangle$ [Eq. (14)]. They can give unique insights into the domain distribution, which is also highly interesting for ultrafast switching experiments.

As a proof of concept, we probe the nonsaturated sample state during the quasistatic reversal of $\boldsymbol{L}$ in an external magnetic field, as shown in Fig. 7(a), which is analogous to Fig. 3(b). In the discussion in Sec. III A 2, several features of this reversal were pointed out, e.g., the nucleation of $\boldsymbol{u}_y$ domains. In the following, we evaluate whether THz-pump optical-probe experiments can confirm these conclusions and provide even further insights into the exact domain distribution.

In general, there are two in-plane easy axes for the Néel vector and, consequently, four distinct directions. Thus a multidomain state can be described by four fractions

$$f_{\varphi_{L_0}} = \frac{V_{\varphi_{L_0}}}{V}, \tag{17}$$

of the total probed volume V. Here, $V_{\varphi_{L_0}}$ is the volume with angle $\varphi_{L_0} = 0^\circ,\ 90^\circ,\ 180^\circ$ and 270° of $\boldsymbol{L}$ relative to the easy direction $\boldsymbol{u}_x$. The fractions fulfill

$$\sum_{\varphi_{L_0}} f_{\varphi_{L_0}} = 1. \tag{18}$$

1. Scaling of quasistatic signals

For a multi-domain state within the probed volume, the quasistatic signal is determined by Eq. (6) and can be written as

$$\langle R_0 \rangle = r_L L_0^2 \langle \cos(2\varphi_{L_0}) \rangle = r_L L_0^2 \sum_{\varphi_{L_0}} f_{\varphi_{L_0}} \cos(2\varphi_{L_0}). \tag{19}$$

Because we have $\cos(2\varphi_{L_0}) = +1$ for horizontal domains ($\varphi_{L_0} = 0^\circ, 180^\circ$), $\cos(2\varphi_{L_0}) = -1$ for vertical domains ($\varphi_{L_0} = 90^\circ,\ 270^\circ$), Eq. (19) with Eq. (18) becomes

$$\langle R_0 \rangle = r_L L_0^2 [2(f_{0^\circ} + f_{180^\circ}) - 1]. \tag{20}$$

As indicated in the schematic of Fig. 7(a), for saturation at $B_{\mathrm{ext}}(t) = -B_{\mathrm{ext}0}$, we can assume $f_{180^\circ} = 1$ and, likewise, $f_{0^\circ} = 1$ at $B_{\mathrm{ext}}(t) = +B_{\mathrm{ext}0}$. Both cases yield a signal $\langle R_0 \rangle = r_L L_0^2$. In contrast, at times t during switching, $\langle R_0 \rangle \approx 0$ indicates the presence of 90° and 270° domains, and one may expect a roughly equal distribution among the four orientations.

To facilitate an elegant comparison with the pump-probe signals in the following, we further separate the signal $\langle R_0 \rangle$ into components

$$\langle R_0^{\pm}(\boldsymbol{B}_{\mathrm{ext}}) \rangle := \frac{\langle R_0(\boldsymbol{B}_{\mathrm{ext}}) \rangle \pm \langle R_0(-\boldsymbol{B}_{\mathrm{ext}}) \rangle}{2} \tag{21}$$

that are even ($\langle R_0^+ \rangle$) and odd ($\langle R_0^- \rangle$) in the external field $\boldsymbol{B}_{\mathrm{ext}}$. Note that $\langle R_0^+ \rangle \approx \langle R_0 \rangle$, while $\langle R_0^- \rangle \approx 0$, i.e., the quasistatic signal is predominantly even in the external magnetic field. Therefore, we can rearrange Eq. (20) as

$$\frac{1}{2}\left(1 \pm \frac{\langle R_0^+ \rangle}{r_L L_0^2}\right) = \begin{cases} f_{0^\circ} + f_{180^\circ} \\ f_{90^\circ} + f_{270^\circ} \end{cases}, \tag{22}$$

where the $\pm$ sign on the left-hand side refers to the top and bottom line on the right-hand side, respectively. The domain-volume fractions parallel to the x axis ($f_{0^\circ} + f_{180^\circ}$) and the y axis ($f_{90^\circ} + f_{270^\circ}$) as extracted by Eq. (22) are shown in Fig. 7(b) versus $B_{\mathrm{ext}}/B_{\mathrm{ext}0}$. Because the MCB signal R_0 is quadratic in $\boldsymbol{L}_0$, it cannot distinguish between domains with Néel vector $\pm\boldsymbol{L}_0$, as also implied by Eq. (22). Therefore, no statement about the exact domain configuration is possible. To mitigate this lack of information, we add THz-pump optical-probe signals at various times t to our analysis.

2. Pump-probe measurements for various magnetic configurations

We now investigate how the pump-probe signals depend on the magnetic sample configuration that is present at the arrival time of the THz pump pulse. The magnetic configuration cycles periodically with period $2T$ of the external field $\boldsymbol{B}_{\mathrm{ext}}(t) = B_{\mathrm{ext}}(t)\boldsymbol{u}_x$. Thus, arbitrary states can be probed by adjusting the timing of the pump-probe experiment with respect to $\boldsymbol{B}_{\mathrm{ext}}(t)$. As summarized in Sec. II B 3 and Figs. 1(d) and 1(e), the THz pump pulse arrives at times $t_{\mathrm{pu}} = t_0$ and $t_{\mathrm{pu}} = t_0 + T$, where $B_{\mathrm{ext}}(t_0)$ and $B_{\mathrm{ext}}(t_0 + T) = -B_{\mathrm{ext}}(t_0)$ have opposite values. Note that the external magnetic field is static for the pump-probe delay $|\tau| \ll T$ used in our experiment, i.e., $B_{\mathrm{ext}}(t_{\mathrm{pu}} + \tau) = B_{\mathrm{ext}}(t_{\mathrm{pu}})$.

To reduce measurement time and probe the magnetic state vs applied field $B_{\mathrm{ext}}(t)$ with fine t resolution, we measure only the minimum number of signals necessary to separate all contributions. We do not reverse the THz electric field, either, since signals odd in only either F or $\boldsymbol{B}_{\mathrm{ext}}$ are negligible on the timescales of the antiferromagnetic mode (Figs. S5 and S6 [17]). As detailed in Appendix B 2, for $\varphi_{\mathrm{pr}} = 45^\circ$ and rotation signals, we use the approximation

$$\langle \Delta R^+ \rangle \approx \frac{\Delta S(F, +B_{\mathrm{ext}}) + \Delta S(F, -B_{\mathrm{ext}})}{2}, \tag{23}$$

while for ellipticity signals that change sign between $\varphi_{\mathrm{pr}} = 0^\circ$ and $\varphi_{\mathrm{pr}} = 90^\circ$, we employ

$$\langle \Delta Q^- \rangle \approx \frac{\Delta S(F, +B_{\mathrm{ext}}) - \Delta S(F, -B_{\mathrm{ext}})}{2}. \tag{24}$$

The opposite field of $B_{\mathrm{ext}}(t)$ is simply obtained by considering the signal at time $t + T$ where $B_{\mathrm{ext}}(t + T) = -B_{\mathrm{ext}}(t)$.

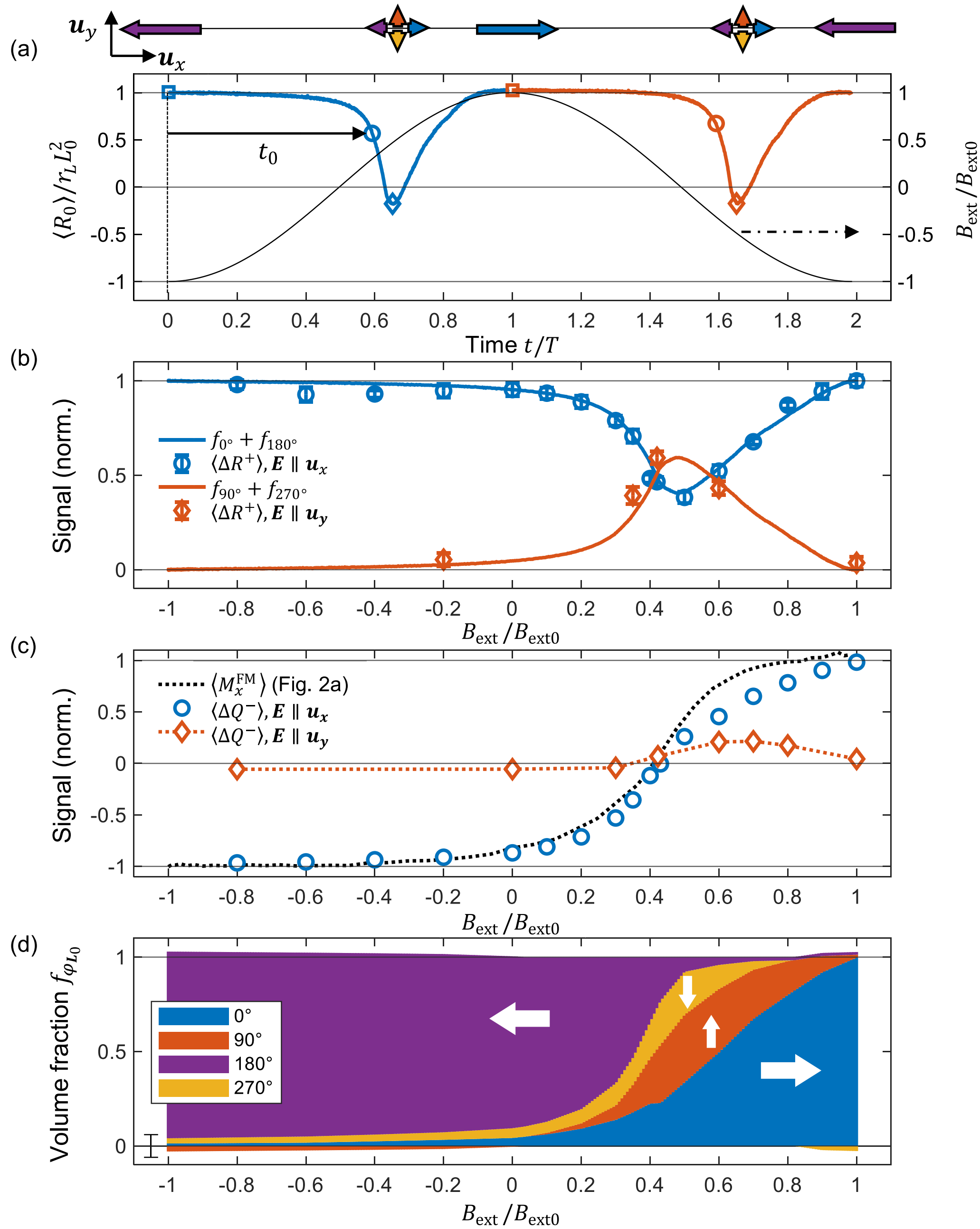

FIG. 7. Probing domain statistics. (a) Concept of the experiment. The top schematic displays the expected qualitative domain distribution when the amplitude $B_{\mathrm{ext}}(t)$ of the external magnetic field $\boldsymbol{B}_{\mathrm{ext}} = B_{\mathrm{ext}}\boldsymbol{u}_x$ increases quasistatically from $-B_{\mathrm{ext0}}$ at $t = 0$ to $+B_{\mathrm{ext0}}$ at $t = T = 1$ ms and subsequently returns to $-B_{\mathrm{ext0}}$ at $t = 2T$ (solid black line). The graph shows $\langle\cos(2\varphi_{L_0})\rangle = \langle R_0\rangle/r_L L_0^2$ for one cycle of increasing (blue line) and decreasing (orange line) B_{ext}, analogous to Fig. 3(b). To characterize the domain volume fractions $f_{0°}$, $f_{90°}$, $f_{180°}$, $f_{270°}$ at a given time t_0, we separately apply THz NSOT to domains with $\boldsymbol{L}_0 \parallel \boldsymbol{u}_x$ and $\boldsymbol{L}_0 \parallel \boldsymbol{u}_y$ and probe magneto-optically. The THz pump pulses arrive at times $t_{\mathrm{pu}} = t_0$ and $t_{\mathrm{pu}} = t_0 + T$. Matching symbols indicate t_{pu} instances, e.g., $t_{\mathrm{pu}} = 0$ (blue square) and $t_{\mathrm{pu}} = T$ (orange square), where $B_{\mathrm{ext}} = \pm B_{\mathrm{ext0}}$. (b) Pump-probe signal amplitude $\langle\Delta R^+\rangle$ even in B_{ext} and, thus, driving THz field vs amplitude B_{ext} for electric field $\boldsymbol{E} \parallel \boldsymbol{u}_x$ (blue circles) and $\boldsymbol{E} \parallel \boldsymbol{u}_y$ (orange diamonds) (Fig. S11 [17]). For comparison, the volume fractions $f_{0°} + f_{180°}$ (blue line) and $f_{90°} + f_{270°}$ (orange line) as derived from quasistatic signals $\langle R_0^+\rangle$ are also shown [Eq. (22)]. (c) Amplitude of $\langle\Delta Q^-\rangle$ for electric field $\boldsymbol{E} \parallel \boldsymbol{u}_x$ (blue circles) and $\boldsymbol{E} \parallel \boldsymbol{u}_y$ (orange diamonds, see Fig. S12 [17]). For comparison, the average magnetization $\langle M_x^{\mathrm{FM}}\rangle$ of layer FM from Fig. 3(a) is shown by the black-dashed line. (d) Extracted volume fractions $f_{0°}$, $f_{90°}$, $f_{180°}$ and $f_{270°}$ of domains in the four easy-axis directions vs B_{ext}. The $f_{\varphi_{L_0}}$ are obtained by combining the amplitude of quasistatic signals in (a) and the pump-probe signals in (c) according to Appendix B 5. White arrows indicate the direction of the Néel vector $\boldsymbol{L}_0$. The bar (bottom left) indicates the uncertainty resulting from the small offset in the orange curve of (c).

3. Scaling of pump-probe signals

NSOT is proportional to the product $\boldsymbol{L}\cdot\boldsymbol{E}$ [14,42] and, thus, $\boldsymbol{L}_0\cdot\boldsymbol{E}$ in the linear-response limit considered here. Therefore, within a single $\boldsymbol{L}_0$ domain, the resulting deflection of the Néel vector scales according to $\Delta\varphi_{\boldsymbol{L}} \propto \boldsymbol{L}_0\cdot\boldsymbol{E} \propto \cos\varphi_{\boldsymbol{L}_0}E_x + \sin\varphi_{\boldsymbol{L}_0}E_y$. In particular, a reversal of the Néel vector ($+\boldsymbol{L}_0 \to -\boldsymbol{L}_0$) leads to response reversal ($+\Delta\varphi_{\boldsymbol{L}} \to -\Delta\varphi_{\boldsymbol{L}}$), while $\Delta\varphi_{\boldsymbol{L}} \approx 0$ for $\boldsymbol{L}_0 \perp \boldsymbol{E}$ [14,42].

Signal $\langle\Delta R^+\rangle$. As a consequence, the pump-probe signal $\langle\Delta R^+\rangle$ [Eq. (14)] is expected to follow

$$\langle\Delta R^+\rangle = 2r_{\boldsymbol{L}}L_0^2\big[(f_{0^\circ}+f_{180^\circ})\big(\Delta\varphi_{\boldsymbol{L}}^x\big)^2 - (f_{90^\circ}+f_{270^\circ})\big(\Delta\varphi_{\boldsymbol{L}}^y\big)^2\big], \tag{25}$$

where $\Delta\varphi_{\boldsymbol{L}}^j(t) = (H_{\Delta\varphi_L\leftarrow E_j} * E_j)(t)$ is the time-dependent deflection of the Néel vector by the THz electric-field component E_j with $j = x, y$ (Table II). Equation (25) implies that the signal amplitude for the two orthogonal pump fields should scale according to

$$\langle\Delta R^+\rangle \propto \begin{cases} +(f_{0^\circ}+f_{180^\circ}) & \text{for} \quad \boldsymbol{E}\parallel \boldsymbol{u}_x \\ -(f_{90^\circ}+f_{270^\circ}) & \text{for} \quad \boldsymbol{E}\parallel \boldsymbol{u}_y \end{cases}. \tag{26}$$

The proportionality factor in Eq. (26) can simply be determined by taking the signal $\langle\Delta R^+\rangle|_{\text{sat}}$ for $\boldsymbol{E}\parallel\boldsymbol{u}_x$ in the magnetically saturated state (sat), i.e., $B_{\text{ext}} = B_{\text{ext0}}$, where $f_{0^\circ} \approx 1$ or $f_{180^\circ} \approx 1$.

The amplitudes of the measured traces $\langle\Delta R^+(\tau)\rangle$ are determined by a projection method (Appendix B 4 and Fig. S11 [17]). The resulting relative amplitude $\langle\Delta R^+\rangle/\langle\Delta R^+\rangle|_{\text{sat}}$ with respect to the signal at maximum external field B_{ext0} versus $B_{\text{ext}}/B_{\text{ext0}}$ are shown in Fig. 7(b). We find that $\langle\Delta R^+\rangle$ for $\boldsymbol{E}\parallel\boldsymbol{u}_x$ and $f_{0^\circ}+f_{180^\circ}$ as obtained through static measurements [Sec. III C 1 and Eq. (22)] agree excellently. Likewise, Fig. 7(b) confirms that, for $\boldsymbol{E}\parallel\boldsymbol{u}_y$, $\langle\Delta R^+\rangle \propto f_{90^\circ}+f_{270^\circ}$, in agreement with Eq. (26). We conclude that $\langle\Delta R^+\rangle$ is dominated by spin degrees of freedom, and $\langle R_0^+\rangle$ and $\langle\Delta R^+\rangle$ report consistently on the domain statistics. However, neither of the signals is able to distinguish $\pm\boldsymbol{L}_0$ domains.

Signal $\langle\Delta Q^-\rangle$. Consequently, we consider the signal contribution $\langle\Delta Q^-\rangle$. By explicitly performing the volume averaging in Eq. (12), we obtain the relationship

$$\langle\Delta Q^-\rangle = 2q_{\boldsymbol{L}}L_0^2\big[(f_{0^\circ}-f_{180^\circ})\Delta\varphi_{\boldsymbol{L}}^x - (f_{90^\circ}-f_{270^\circ})\Delta\varphi_{\boldsymbol{L}}^y\big] \tag{27}$$

and, thus,

$$\langle\Delta Q^-\rangle \propto \begin{cases} +(f_{0^\circ}-f_{180^\circ}) & \text{for} \quad \boldsymbol{E}\parallel \boldsymbol{u}_x \\ -(f_{90^\circ}-f_{270^\circ}) & \text{for} \quad \boldsymbol{E}\parallel \boldsymbol{u}_y \end{cases}. \tag{28}$$

Therefore, both $\langle\Delta Q^-\rangle$ [Eq. (28)] and $\langle\Delta R^+\rangle$ [Eq. (26)] report on the temporal dynamics of $\Delta\varphi_{\boldsymbol{L}}$, but the dependence on the quasistatic domain distribution is complementary and scales like $f_{0^\circ} \pm f_{180^\circ}$ vs $f_{90^\circ} \pm f_{270^\circ}$. Note that the minus sign in front of f_{180° in Eq. (28) arises because $\Delta\varphi_{\boldsymbol{L}}$ reverses as $\boldsymbol{L}_0$ reverses.

Figure 7(c) displays the signal amplitude of $\langle\Delta Q^-\rangle$ (see Fig. S12 [17]). For $\boldsymbol{E}\parallel\boldsymbol{u}_x$, the zero-crossing of $\langle\Delta Q^-\rangle$ indicates $\boldsymbol{L}$ reversal when $B_{\text{ext}} \approx 0.5B_{\text{ext0}}$, consistent with the behavior observed in $\langle R_0^+\rangle$ and $\langle\Delta R^+\rangle$ [Fig. 7(b)]. Remarkably, the amplitude of $f_{0^\circ}-f_{180^\circ} \propto \langle L_x\rangle$ is in very good agreement with the quasistatic signals $\propto \langle M_x^{\text{FM}}\rangle$ [Fig. 3(a)]. The agreement indicates that $\boldsymbol{M}^{\text{FM}}$ and $\boldsymbol{L}$ remain parallel throughout the reversal at the variation rate of B_{ext} employed in our experiment. For $B_{\text{ext}} > 0.5B_{\text{ext0}}$, a signal $\langle\Delta Q^-\rangle \propto f_{90^\circ}-f_{270^\circ} \neq 0$ is observed [Fig. 7(c)]. For $\boldsymbol{E}\parallel\boldsymbol{u}_y$, $\langle\Delta Q^-\rangle$ is nonzero even in the saturated state [$B_{\text{ext}} \approx B_{\text{ext0}}$, Fig. 7(b)]. This finding indicates that $\boldsymbol{E}$ is not exactly perpendicular to the antiferromagnetic easy axis and, thus, exerts NSOT.

4. Full domain statistics

We have now gathered all information to estimate the volume fractions f_{0°, f_{90°, f_{180° and f_{270° of the four domains at any time t and, thus, $B_{\text{ext}}(t)$. To achieve this goal, we use Eq. (18) and, thus, need only three independent observables from our measurements of $\langle R_0^+\rangle$ and $\langle\Delta Q^-\rangle$ with $\boldsymbol{E}\parallel\boldsymbol{u}_x$ and $\boldsymbol{E}\parallel\boldsymbol{u}_y$, respectively (see Appendix B 5). The individual domain fractions are subsequently obtained by linear combination of the observables.

Figure 7(d) shows the extracted domain-volume fractions vs external field $B_{\text{ext}}/B_{\text{ext0}}$, where the data are interpolated on a finer grid for better visibility. For $B_{\text{ext}} = -0.8B_{\text{ext0}}$, virtually all domains are at 180° with respect to $\boldsymbol{u}_x$, i.e., $f_{180^\circ} = 1$. Our extraction procedure of f_{0°, f_{90°, f_{180° and f_{270° is subject to systematic uncertainties due to imperfect alignment of $\boldsymbol{E}$, which, in our case manifests itself in a small negative fraction f_{90° at $B_{\text{ext}} = -0.8B_{\text{ext0}}$.

Upon increasing B_{ext} toward zero, the fraction of 0°, 90° and 270° domains starts growing. Interestingly, at $B_{\text{ext}} = 0.5B_{\text{ext0}}$, a small dominance of the 90° and 270° domains is observed, i.e., $f_{90^\circ}+f_{270^\circ} > f_{0^\circ}+f_{180^\circ}$. Thus, the expected distribution sketched in Fig. 3(b) is largely reproduced. However, our probe approach can distinguish 90° and 270° domains and reveals a small preference for the nucleation of the 90° type in the half-cycle of $B_{\text{ext}}(t)$ shown in Fig. 7(d). We attribute this behavior to $\boldsymbol{B}_{\text{ext}}$ not being perfectly parallel or perpendicular to the two easy axes, which favors nucleation of domains that align better with $\boldsymbol{B}_{\text{ext}}$ [43].

IV. SUMMARY AND DISCUSSION

Signals are dominated by spins. We measure magneto-optic signals for quasistatic and ultrafast variations of the magnetic order of an exchange-coupled AFM|FM system. Importantly, we find that all signals predominantly report on true spin dynamics, including signals even in $\boldsymbol{L}_0$. More precisely, the observed MLB signals report on the dynamic Néel-vector deflection $\Delta\varphi_{\boldsymbol{L}}$ in linear and quadratic order, i.e., $\langle\Delta Q^-(t)\rangle \propto \Delta\varphi_{\boldsymbol{L}}(t)$ [Eq. (12)] and $\langle\Delta R^+(t)\rangle \propto [\Delta\varphi_{\boldsymbol{L}}(t)]^2$ [Eq. (14)]. Therefore, the observed signals $\langle\Delta R^+(t)\rangle$ quadratic in the driving THz field result exclusively from the probing mechanism, while the spin dynamics $\Delta\varphi_{\boldsymbol{L}}(t)$ are still in the linear-response regime.

The complementary information content of $\langle\Delta Q^-(t)\rangle$ and $\langle\Delta R^+(t)\rangle$ permits the identification of pure spin dynamics and even the calibration of the amplitude of $\Delta\varphi_{\boldsymbol{L}}(t)$ [Eq. (15)]. In this context, we note that MLB signals, as opposed to MCB, are appropriate tools to probe the antiferromagnetic dynamics in Mn_2Au, as they yield larger signals in typical situations where $|\Delta\boldsymbol{M}^{\text{AFM}}| \ll |\boldsymbol{L}_0|$.

To summarize, the ultrafast pump-induced signals have precisely the same interpretation as the signals for quasistatic variation of $\boldsymbol{L}$ and $\boldsymbol{M}$ by an external magnetic field [Eqs. (6) and (12)–(14)]. This analogy indicates that the pump-induced signals can be transferred from the small-signal response to the general response as with the quasistatic case, i.e.,

$$\langle \Delta Q^- \rangle \propto L_0^2 \langle \Delta \sin(2\varphi_L) \rangle \quad \text{and} \quad \langle \Delta R^+ \rangle \propto L_0^2 \langle \Delta \cos(2\varphi_L) \rangle. \tag{29}$$

The complementary information of the dynamics probed by $\langle \Delta Q^- \rangle$ and $\langle \Delta R^+ \rangle$ is expected to become essential in the highly nonlinear and, ultimately, ultrafast switching regime. For example, assuming $\varphi_{L_0} = 0^\circ$, a transient signal $\langle \Delta \sin(2\varphi_L) \rangle$ would be zero for $\varphi_L(t) = 0^\circ$, 90°, 180° and 270°, whereas $\langle \Delta \cos(2\varphi_L) \rangle$ would be able to distinguish $\varphi_L(t) = 0^\circ, 180^\circ$ from $\varphi_L(t) = 90^\circ, 270^\circ$.

Exchange-coupled AFM and FM. Both the quasistatic signals (Figs. 2 and 3) and ultrafast signals (Fig. 7) show clear indications that the ferromagnetic magnetization $\boldsymbol{M}^{\mathrm{FM}}$ and Néel vector $\boldsymbol{L}$ are jointly controlled by the external magnetic field $\boldsymbol{B}_{\mathrm{ext}}$. This notion is in excellent agreement with previous results [16]. The exchange coupling of AFM and FM results in identical coercive-field values in both layers (Fig. 3), but no exchange bias of the ferromagnet [Fig. 3(a)]. A thin insulating spacer layer fully suppresses the exchange coupling and, thus, also emphasizes the importance of the interface quality [Fig. 2(b)]. Importantly, our method enables fast, robust and isothermal *in situ* control of antiferromagnetic order and is highly desired for future experiments of ultrafast switching.

Spin torques and temporal dynamics. The observed spin dynamics are very well explained by the in-plane antiferromagnetic magnon mode within the σ-model, which dictates a strict relationship between the dynamics of the Néel vector and the net magnetization [Fig. 5(c) and Eq. (10)]. The mode is driven predominantly by NSOT, and the amplitude calibration allows for the extraction of the torkance, which is in good agreement with previous results [14].

These results indicate that the presence of layer FM in the exchange-coupled system AFM|FM preserves the general characteristics of the spin dynamics in layer AFM. We note, however, that an even better fit of the data in Fig. 5(a) can be obtained by a superposition of two sinusoidal modes as a response (Fig. S13 [17]). This fact may indicate the presence of an inhomogeneous standing spin wave in AFM due to the exchange coupling with layer FM. A related effect was observed in the spin dynamics of layer FM by ferromagnetic-resonance experiments [15].

Other signal contributions. In our presentation, we have focused largely on results that can be explained entirely by the antiferromagnetic dynamics. Here, we address the remaining features of the dynamic response. First, there is a fast feature in the ellipticity-type $\langle \Delta R^+(t) \rangle$ that resembles the square $\boldsymbol{E}^2(t)$ of the THz field. We tentatively attribute this component to an anisotropic electron distribution in momentum space of AFM or FM, which relaxes with the momentum relaxation time of $\sim$10 fs [41].

Second, the MCB signal $\langle \Delta P^- \rangle$ is expected to also contain a contribution due the change ΔM_z^{FM} in the FM magnetization, driven by off-resonant Zeeman torque [19]. The rotation part of $\langle \Delta P^- \rangle$ contains a contribution that is consistent with this scenario (Fig. S8 [17]). Third, in the rotation signal $\langle \Delta Q^- \rangle$ (Fig. S8 [17]), we find an additional fast component that follows the temporal waveform of the THz pump field.

Domain statistics during switching. An interesting feature of the quasistatic reversal shown in Fig. 7(b) is that both quasistatic and pump-probe signals consistently indicate an imbalance $f_{90^\circ} + f_{270^\circ} > f_{0^\circ} + f_{180^\circ}$ at $B_{\mathrm{ext}} = 0.5 B_{\mathrm{ext0}}$. As the extraction methods are independent of each other, we conclude that this imbalance is not due to a systematic offset in either method. The imbalance rather indicates that the nucleation and growth of 90° and 270° domains plays a major role in the Néel-vector reversal, potentially in combination with local strains favoring these orientations [44,45].

There is a second imbalance $f_{90^\circ} > f_{270^\circ}$ at $B_{\mathrm{ext}} = 0.5 B_{\mathrm{ext0}}$ [Fig. 7(d)]. This feature may arise from a small nonzero angle between the external magnetic field $\boldsymbol{B}_{\mathrm{ext}}$ and the magnetic easy axes, causing a preferential nucleation of the 90° domains in our experiment.

V. CONCLUSION

First, we show that AFM|FM exchange-coupled systems serve as good model systems for antiferromagnetic spintronics, thereby providing external control of the Néel vector $\boldsymbol{L}$ without significant alteration of the ultrafast dynamics. It is, therefore, highly interesting to identify such systems for the study of antiferromagnets or altermagnets [46]. Our approach can help to uniquely determine magnetic-order-related effects in such materials.

In this context, we stress that a single macroscopic $\boldsymbol{L}$ domain can only be formed in exchange-coupled systems where the antiferromagnet terminates with the same type of spin sublattice at the interface [16] or, equivalently, allows for an uncompensated surface magnetization. A recent theoretical study indicates that this so-called roughness-robust surface magnetization can be realized in a wider range of antiferromagnets and altermagnets [47]. In combination with suitable ferromagnetic capping layers, such materials may also form AFM|FM exchange-coupled systems that provide extended control over the antiferromagnetic order by external fields. In these cases, the methods developed here will be very useful for the characterization of magnetic order, magneto-optic properties, and ultrafast spin dynamics.

Second, our results reveal that THz pulses allow one to implement NSOT-based probing that is sensitive to the direction, i.e., orientation, and not only the alignment of $\boldsymbol{L}$, in contrast to commonly used techniques, like x-ray magnetic linear dichroism [13]. Our probing is applicable to bare antiferromagnets beyond exchange-coupled systems. More generally, our experiment is a special realization of a second-order optical response of the sample. It is, thus, similar to other nonlinear optical techniques, such as second-harmonic generation [48], but explicitly takes advantage of resonant THz magnon excitation.

For the potential study of ultrafast coherent switching of $\boldsymbol{L}$ in Mn_2Au, we found solutions to the challenges (C1) and (C2) outlined in Sec. I: (C1) external control of $\boldsymbol{L}$, and (C2) exploration and calibration of magneto-optic responses of Mn_2Au.

We are, thus, left with the final step of (C3) increasing the NSOT magnitude, e.g., by employing high-field THz sources [49] or resonant microstructure antennas [2,50].

ACKNOWLEDGMENTS

The authors acknowledge funding by the the DFG Excellence Cluster EXC 3112 “Center for Chiral Electronics” (EXC 3112/1, Project No. 533767171), the DFG Research Unit RU 5844 ChiPS (Project No. 541503763), the DFG collaborative research center SFB TRR 227 “Ultrafast spin dynamics” (project ID 328545488, projects A05 and B02), the DFG collaborative research center SFB TRR 173 “Spin+X” (project ID 268565370, projects A01, A05 and B02), the DFG Major Research Instrumentation Grant No. INST 130/1268-1 FUGG, by ERC-2023-AdG ORBITERA/Grant No. 101142285, ERC-2019-SyG 3D MAGiC/Grant No. 856538 and MSCA ITN MagnEfi/Grant No. 860060.

DATA AVAILABILITY

The data that support the findings in the article are openly available [51]. The data for the Supplemental Materials are available upon reasonable request from the authors.

APPENDIX A: SIGNAL PHENOMENOLOGY

In this Appendix, we derive the general signal equation [Eq. (5)] for our experiment and its constituents (Table I).

1. Local currents and symmetry

Generally, the electric field $\boldsymbol{E}_{\mathrm{pr}}$ of an optical probe pulse induces a charge-current density $\boldsymbol{j}_{\mathrm{pr}}$ in the sample [Fig. 1(a)]. In the frequency domain, the current is given by

$$\boldsymbol{j}_{\mathrm{pr}}(\boldsymbol{r},\omega)=\underset{\sim}{\sigma}(\boldsymbol{r},\omega)\boldsymbol{E}_{\mathrm{pr}}(\boldsymbol{r},\omega), \tag{A1}$$

where $\boldsymbol{r}=(x,y,z)$ is the spatial position, $\omega/2\pi$ is the frequency, and $\underset{\sim}{\sigma}$ is the optical conductivity tensor. In general, the three terms in Eq. (A1) are complex-valued. Further, they quasistatically depend on external electric and magnetic fields, which are much slower than the probe-pulse duration and, thus, $2\pi/\omega$. For the sake of simplicity, the arguments $\boldsymbol{r}$, ω and any time dependence are often omitted in the following.

The optical conductivity tensor can be decomposed as [14]

$$\underset{\sim}{\sigma}=\underset{\sim}{\sigma}_0+\Delta\underset{\sim}{\sigma}(\boldsymbol{E},\boldsymbol{B},\boldsymbol{M},\boldsymbol{L}), \tag{A2}$$

where $\underset{\sim}{\sigma}_0$ is the conductivity in the absence of external electric and magnetic fields $(\boldsymbol{E},\boldsymbol{B})$ and of magnetic order $(\boldsymbol{M},\boldsymbol{L})$. It is solely determined by the local crystallographic symmetry. The second term of Eq. (A2) quantifies the changes resulting from external fields and magnetic order in the sample. It can be further separated into [14]

$$\Delta\underset{\sim}{\sigma}=\Delta\underset{\sim}{\sigma}_{\mathcal{N}}+\Delta\underset{\sim}{\sigma}_{\mathcal{S}}, \tag{A3}$$

where $\Delta\underset{\sim}{\sigma}_{\mathcal{N}}$ refers to changes introduced by the non-spin degrees of freedom $\mathcal{N}$, while $\Delta\underset{\sim}{\sigma}_{\mathcal{S}}$ refers to changes in the spin degrees of freedom $\mathcal{S}$.

Probe field. In our experiment [Fig. 1(a)], the probe pulse with field $\boldsymbol{E}_{\mathrm{pr}}$ arrives at the sample under normal incidence and drives a current $\boldsymbol{j}_{\mathrm{pr}}$ [Eq. (A1)]. The current due to $\Delta\underset{\sim}{\sigma}$ emits an additional light field $\Delta\boldsymbol{E}_{\mathrm{pr}}$ that superimposes with the field $\boldsymbol{E}_{\mathrm{pr0}}$ obtained for the unperturbed sample with $\Delta\underset{\sim}{\sigma}=0$. In the laboratory frame, the pulse propagates along $\boldsymbol{u}_z$. For $|\Delta\boldsymbol{E}_{\mathrm{pr}}|\ll|\boldsymbol{E}_{\mathrm{pr0}}|$ and a laterally homogeneous sample, the $\Delta\underset{\sim}{\sigma}$-induced field directly behind the sample film of thickness d is given by [52]

$$\Delta\boldsymbol{E}_{\mathrm{pr}}(d,\omega)=\int_0^d \mathrm{d}z'\, g(d,z',\omega)\Delta\boldsymbol{j}_{\mathrm{pr}\perp}. \tag{A4}$$

In Eq. (A4), $g(d,z',\omega)$ is the scalar electromagnetic Green's function, and $\Delta\boldsymbol{j}_{\mathrm{pr}\perp}$ is the projection of the $\Delta\underset{\sim}{\sigma}$-related probe current $\Delta\boldsymbol{j}_{\mathrm{pr}}=\Delta\underset{\sim}{\sigma}\boldsymbol{E}_{\mathrm{pr0}}$ onto the plane perpendicular to the probe propagation direction $\boldsymbol{u}_{\mathrm{pr}}=\boldsymbol{u}_z$ [52].

2. Polarimetric signal

To interrogate $\Delta\underset{\sim}{\sigma}$, we use a linearly polarized incident probe pulse and detect $\Delta\boldsymbol{E}_{\mathrm{pr}}$ by the balanced polarimetric detection scheme shown in Fig. S14 [17]. The resulting polarimetric signal scales linearly with $\Delta\boldsymbol{E}_{\mathrm{pr}}$ and can, in the case of the probe-polarization rotation (rot), compactly be written as

$$S_{\mathrm{rot}}\propto \mathrm{Re}\int_0^\infty \mathrm{d}\omega\,[\boldsymbol{E}_{\mathrm{pr0}}(d,\omega)^*\times\Delta\boldsymbol{E}_{\mathrm{pr}}(d,\omega)]\cdot\boldsymbol{u}_z. \tag{A5}$$

According to Eq. (A5), S_{rot} is only nonzero if $\Delta\boldsymbol{E}_{\mathrm{pr}}(d,\omega)$ is not parallel to $\boldsymbol{E}_{\mathrm{pr0}}(d,\omega)$, i.e., when the polarization of $\boldsymbol{E}_{\mathrm{pr0}}+\Delta\boldsymbol{E}_{\mathrm{pr}}$ is different from $\boldsymbol{E}_{\mathrm{pr0}}$. Further, if $\boldsymbol{E}_{\mathrm{pr0}}$ and $\Delta\boldsymbol{E}_{\mathrm{pr}}(d,\omega)$ are out of phase by 90°, $\boldsymbol{E}_{\mathrm{pr0}}+\Delta\boldsymbol{E}_{\mathrm{pr}}$ is elliptically polarized but not rotated relative to $\boldsymbol{E}_{\mathrm{pr0}}$, and S_{rot} vanishes.

To measure the signal S_{ell} due to the acquired probe ellipticity (ell), we simply phase-shift $\Delta\boldsymbol{E}_{\mathrm{pr}}$ by −90° into phase with $\boldsymbol{E}_{\mathrm{pr0}}$ by means of a quarter-wave plate before the polarizing beam splitter (Fig. S14 [17]). Therefore, to express S_{ell} by a relation analogous to Eq. (A5), we just need to substitute $S_{\mathrm{rot}}\to S_{\mathrm{ell}}$ and $\Delta\boldsymbol{E}_{\mathrm{pr}}\to -\mathrm{i}\Delta\boldsymbol{E}_{\mathrm{pr}}$ in Eq. (A5). The resulting S_{ell} and S_{rot} can elegantly be summarized by the complex-valued polarimetric signal

$$S_{\mathrm{rot}}+\mathrm{i}S_{\mathrm{ell}}\propto\int_0^\infty \mathrm{d}\omega\,[\boldsymbol{E}_{\mathrm{pr0}}(d,\omega)^*\times\Delta\boldsymbol{E}_{\mathrm{pr}}(d,\omega)]\cdot\boldsymbol{u}_z. \tag{A6}$$

To explicitly relate the signal to the desired $\Delta\underset{\sim}{\sigma}$, we assume that the principal optical axes $\boldsymbol{u}_1,\boldsymbol{u}_2,\boldsymbol{u}_3$ of the unperturbed sample with $\Delta\underset{\sim}{\sigma}=0$ align with the laboratory directions $\boldsymbol{u}_x,\boldsymbol{u}_y,\boldsymbol{u}_z$. This assumption is justified for tetragonal Mn_2Au and the effectively isotropic Py (Table IV), where $\sigma_{0,ij}=\sigma_0\delta_{ij}$ for $i,j=1,2$. By writing $\boldsymbol{E}_{\mathrm{pr0}}=E_{\mathrm{pr0},1}\boldsymbol{u}_1+E_{\mathrm{pr0},2}\boldsymbol{u}_2$, we obtain $|E_{\mathrm{pr0},1}|^2=|\boldsymbol{E}_{\mathrm{pr0}}|^2\cos^2\varphi_{\mathrm{pr}}$, $|E_{\mathrm{pr0},2}|^2=|\boldsymbol{E}_{\mathrm{pr0}}|^2\sin^2\varphi_{\mathrm{pr}}$ and $2E^*_{\mathrm{pr0},1}E_{\mathrm{pr0},2}=2E^*_{\mathrm{pr0},2}E_{\mathrm{pr0},1}=|\boldsymbol{E}_{\mathrm{pr0}}|^2\sin(2\varphi_{\mathrm{pr}})$, where φ_{pr} is the angle between $\boldsymbol{E}_{\mathrm{pr0}}$ and $\boldsymbol{u}_1=\boldsymbol{u}_x$ (Fig. S14 [17]). With Eqs. (A4) and (A6), we find

$$S_{\mathrm{rot}}+\mathrm{i}S_{\mathrm{ell}}\propto\int_0^d \mathrm{d}z'\int_0^\infty \mathrm{d}\omega\,[P+Q\cos(2\varphi_{\mathrm{pr}})+R\sin(2\varphi_{\mathrm{pr}})]w, \tag{A7}$$

TABLE IV. Symmetry-allowed magnetic tensor components in bulk Mn_2Au and $Ni_{80}Fe_{20}$. Only components relevant for normal incidence are given.

Tensor	Type	Mn_2Au(tetragonal 4/mmm)	$Ni_{80}Fe_{20}$ (Py)(isotropic $\infty\infty$ m)
$\sigma_{0,ij}$	Polar	$\sigma_{0,11} = \sigma_{0,22}$	As 4/mmm
α_{ijk}	Axial	$\alpha_{123} = -\alpha_{213}$	As 4/mmm
β_{ijk}	Axial, staggered	0	As 4/mmm
γ_{ijkl}	Polar	$\gamma_{1111} = \gamma_{2222}$	$\gamma_{1111} = \gamma_{2222}$
		$\gamma_{1122} = \gamma_{2211}$	$\gamma_{1122} = \gamma_{2211}$
		$\gamma_{1212} = \gamma_{1221} = \gamma_{2112} = \gamma_{2121}$	$\gamma_{1212} = \gamma_{1221} = \gamma_{2112} = \gamma_{2121}$ $= \frac{1}{2}(\gamma_{1111} - \gamma_{1122})$
ϵ_{ijkl}	Polar	Same as γ_{ijkl}	Same as γ_{ijkl}

where

$$P = \frac{\Delta\sigma_{21} - \Delta\sigma_{12}}{2},$$
$$Q = \frac{\Delta\sigma_{21} + \Delta\sigma_{12}}{2}, \tag{A8}$$
$$R = \frac{\Delta\sigma_{22} - \Delta\sigma_{11}}{2}.$$

In Eq. (A7), the integration over z' and ω arises from Eqs. (A4) and (A5), respectively. The sensitivity function $w = w(z', \omega)$ scales with the Green's function $g(d, z', \omega)$ and the intensity profile $|\boldsymbol{E}_{\mathrm{pr0}}(z', \omega)|^2$ of the unperturbed probe pulse throughout the sample.

3. Lateral averaging

In our experiment, $\Delta\underline{\sigma}$ can easily be spatially inhomogeneous due, e.g., to variations of the magnetic order parameters and the THz pump field. For the z dimension, this effect is already captured by Eq. (A7). To take a possible x and y dependence of $\Delta\underline{\sigma}$ into account, we expand $\Delta\underline{\sigma}(x, y, z, \omega)$ versus x and y into a superposition of plane waves with wave vectors k_x and k_y. Each component $\Delta\underline{\sigma}(k_x, k_y, z, \omega)$ generates a new wave $\Delta\boldsymbol{E}_{\mathrm{pr}}$ that propagates away from the sample normal ($k_x = k_y = 0$) [53] and, thus, the wave $\boldsymbol{E}_{\mathrm{pr0}}$. Consequently, $\Delta\boldsymbol{E}_{\mathrm{pr}}$ and $\boldsymbol{E}_{\mathrm{pr0}}$ interfere destructively on the detector area, and only components $\Delta\underline{\sigma}(k_x, k_y, z, \omega)$ with $k_x = k_y = 0$ contribute to the measured signal S. Because $\Delta\underline{\sigma}(k_x = 0, k_y = 0, z, \omega) = \iint \mathrm{d}x\,\mathrm{d}y\, \Delta\underline{\sigma}(x, y, z, \omega)$, we just need to add the integration $\iint \mathrm{d}x\,\mathrm{d}y \ldots$ to Eqs. (A6) and (A7).

Further, in the experiment, we divide the pump-induced signal by the total probe-pulse energy $\iint \mathrm{d}x\,\mathrm{d}y \int \mathrm{d}\omega\, |\boldsymbol{E}_{\mathrm{pr0}}(x, y, d, \omega)|^2$ behind the sample. We, thus, obtain the final relationship

$$S_{\mathrm{rot}} + \mathrm{i}S_{\mathrm{ell}} = \langle P\rangle + \langle Q\rangle \cos(2\varphi_{\mathrm{pr}}) + \langle R\rangle \sin(2\varphi_{\mathrm{pr}}), \tag{A9}$$

where the weighted average is given by

$$\langle X\rangle = \iint \mathrm{d}x\,\mathrm{d}y \int_0^d \mathrm{d}z \int_0^\infty \mathrm{d}\omega\, X(x, y, z, \omega) w(x, y, z, \omega). \tag{A10}$$

In this generalization of Eq. (A7), the complex-valued sensitivity function $w(x, y, z, \omega)$ scales with the Green's function $g(d, z, \omega)$, the intensity profile $|\boldsymbol{E}_{\mathrm{pr0}}(x, y, z, \omega)|^2$ of the unperturbed probe pulse throughout the sample volume, and the inverse of the total probe-pulse energy $\iint \mathrm{d}x\,\mathrm{d}y \int \mathrm{d}\omega |\boldsymbol{E}_{\mathrm{pr0}}(x, y, d, \omega)|^2$ behind the sample.

In other words, the angular bracket $\langle . \rangle$ denotes averaging over x, y, ω and integration over z. However, for the sake of simplicity, we refer to $\langle . \rangle$ as average in most of the text. We note that, for the thin films and the transmission geometry of our experiment, $w(x, y, z, \omega)$ is expected to be largely independent of, respectively, the frequency $\omega/2\pi$ across the probe-pulse spectrum and the position z inside the AFM and FM layers [54].

4. Expansion of the conductivity tensor

Finally, to relate the optical conductivity of Eq. (A2) to the spin-related degrees of freedom in our sample, we expand the conductivity up to second order in the time-dependent magnetic order parameters $\boldsymbol{M}$ and $\boldsymbol{L}$,

$$\sigma_{ij} = \sigma_{0,ij} + \Delta\sigma_{\mathcal{N},ij}(\boldsymbol{E}, \boldsymbol{B}) + \sum \alpha_{ijk} M_k + \sum \beta_{ijk} L_k + \sum \gamma_{ijkl} M_k M_l + \sum \epsilon_{ijkl} L_k L_l. \tag{A11}$$

Here, $\Delta\sigma_{\mathcal{N},ij}(\boldsymbol{E}, \boldsymbol{B})$ contains the dynamics of nonspin degrees of freedom $\mathcal{N}$ due to the external electric and magnetic fields [14]. They cannot be separated based on symmetry, as discussed in Sec. II C, and will not be further specified here. The relevant components of the tensors α_{ijk}, β_{ijk}, γ_{ijkl} and ϵ_{ijkl} are given in Table IV for the case of tetragonal Mn_2Au (point group 4/mmm) and effectively isotropic Py ($Ni_{80}Fe_{20}$, point group $\infty\infty$m). For the two layers, only γ_{ijkl} and ϵ_{ijkl} differ in symmetry. We neglect any symmetry reduction in the vicinity of surfaces and interfaces.

By combining Eqs. (A8), (A9), and (A11) with the allowed tensor components in Table IV, we arrive at the magnetic signal contributions given in Eq. (5) and Table I of the main text. There, we subsume the weighting function and the magneto-optic coefficient into a single prefactor denoted by $(p_{\boldsymbol{M}}, q_{\boldsymbol{L}}, \ldots)$.

5. Signals linear in $\boldsymbol{M}$ and $\boldsymbol{L}$

We conclude the derivation of Table I by commenting on signal contributions that scale linearly with the order parameters $\boldsymbol{M}$ and $\boldsymbol{L}$. First, there is no signal linear in $\boldsymbol{L}$ because $\beta_{ijk} = 0$ in AFM and FM by symmetry (Table IV). Second, there is no signal linear in $\boldsymbol{M}$ for normal probe incidence

[$\boldsymbol{u}_{\rm pr} = \boldsymbol{u}_z$, Fig. 1(a)] and in-plane magnetization ($\boldsymbol{M}\perp\boldsymbol{u}_z$) because $\Delta\boldsymbol{j}_{\rm pr\perp}$ vanishes in this case [Eq. (A4)].

Magneto-optic effects linear in the in-plane part of $\boldsymbol{M}$ can be activated, however, by choosing non-normal probe incidence ($\boldsymbol{u}_{\rm pr} \neq \boldsymbol{u}_z$). The resulting signal contribution proportional to $\langle \boldsymbol{M}\cdot\boldsymbol{u}_{\rm pr}\rangle$ is a generalization of the result $\langle M_z\rangle = \langle \boldsymbol{M}\cdot\boldsymbol{u}_z\rangle$ for normal probe incidence (Table I).

APPENDIX B: EXTRACTION OF SIGNAL COMPONENTS, AMPLITUDES, AND PARAMETERS

This Appendix deals with the extraction of various signal components and model parameters.

1. Extraction of ⟨P⟩, ⟨Q⟩, ⟨R⟩

To extract the MCB contribution $\langle P\rangle$ and the MLB components $\langle Q\rangle$ and $\langle R\rangle$ from the measured signals [Eq. (5)], we note that the functions $\cos(2\varphi_{\rm pr})$, $\sin(2\varphi_{\rm pr})$ and $1=\cos(0\varphi_{\rm pr})$ in Eq. (5) are mutually orthogonal. Consequently, we measure the signals $S(t,n)$ for a set of equidistant probe-polarization angles $\varphi_{{\rm pr},n} = 2\pi n/N$ in the interval $[0,\pi[$ for $n=0,\ldots,N/2-1$, where N is even and $N/2 \geqslant 4$. We assume that, for $n' = N/2,\ldots,N-1$, we can write $S(t,n') = S(t,n'-N)$, i.e., the signals are identical for $\varphi_{\rm pr}$ and $\varphi_{\rm pr}+\pi$.

Because $2\cos(2\varphi_{\rm pr}) = {\rm e}^{{\rm i}2\varphi_{\rm pr}} + {\rm e}^{-{\rm i}2\varphi_{\rm pr}}$, $2{\rm i}\sin(2\varphi_{\rm pr}) = {\rm e}^{{\rm i}2\varphi_{\rm pr}} - {\rm e}^{-{\rm i}2\varphi_{\rm pr}}$, and $1 = {\rm e}^{{\rm i}0\varphi_{\rm pr}}$, the $\langle Q(t)\rangle$, $\langle R(t)\rangle$, and $\langle P(t)\rangle$ are, respectively, given by $[\tilde S(t,2)+\tilde S(t,-2)] = 2{\rm Re}\tilde S(t,2)$, $[\tilde S(t,2)-\tilde S(t,-2)]/{\rm i} = 2{\rm Im}\tilde S(t,2)$, and $\tilde S(t,0)$. Here,

$$\tilde S(t,k) = \frac{1}{N}\sum_{n=0}^{N-1} S(t,n){\rm e}^{-2\pi{\rm i}nk/N} \tag{B1}$$

is the discrete Fourier transformation of $S(t,n)$ with respect to n at integer frequency $k=-N/2,\ldots,N/2-1$. It is the amplitude of the signal component with an angle period of $2\pi/k$. For the quasistatic signals in Fig. 2(a), $N/2=4$ probe polarizations are used (Fig. S2 [17]), while for the signals in Fig. 2(b), Fig. S4 [17], Figs. 5(a) and 6(a), $N/2=8$ polarizations are used (Figs. S5 and S6 [17]).

2. Signals odd and even in external magnetic field

The signal contributions with respect to the external magnetic field $\boldsymbol{B}_{\rm ext}$ can be separated as $\Delta S = \Delta S^+_{\boldsymbol{B}_{\rm ext}} + \Delta S^-_{\boldsymbol{B}_{\rm ext}}$. Here,

$$\Delta S^{\pm}_{\boldsymbol{B}_{\rm ext}} := \frac{\Delta S(F,+\boldsymbol{B}_{\rm ext}) \pm \Delta S(F,-\boldsymbol{B}_{\rm ext})}{2} \tag{B2}$$

is the component even (+) and odd (−) in $\boldsymbol{B}_{\rm ext}$.

For the probe polarization $\varphi_{\rm pr}=45^\circ$, the signal is given by $\Delta S = \langle\Delta P\rangle + \langle\Delta R\rangle$ [Eq. (5)]. As shown in Fig. S5 [17], signals odd in only either F or $\boldsymbol{B}_{\rm ext}$ are negligible, $\langle\Delta P\rangle$ is predominantly odd in $\boldsymbol{B}_{\rm ext}$, and $\langle\Delta R\rangle$ is predominantly even. Thus, for $\varphi_{\rm pr}=45^\circ$, we have $\Delta S^-_{\boldsymbol{B}_{\rm ext}} \approx \langle\Delta P^-\rangle$ and $\Delta S^+_{\boldsymbol{B}_{\rm ext}} \approx \langle\Delta R^+\rangle$.

When probing with $\varphi_{\rm pr}=0^\circ$ and 90°, the signals are $\langle\Delta P\rangle + \langle\Delta Q\rangle$ and $\langle\Delta P\rangle - \langle\Delta Q\rangle$, respectively. Consequently, the signal contribution changing sign is $\langle\Delta Q\rangle$. As shown in Fig. S5 [17], $\langle\Delta Q\rangle$ does not contain contributions odd in $\boldsymbol{B}_{\rm ext}$ and even in F. Therefore, we have $\langle\Delta Q^-_{\boldsymbol{B}_{\rm ext}}\rangle \approx \langle\Delta Q^-\rangle$.

3. RMS amplitude

The noise-adjusted root-mean-square amplitude RMS of a signal waveform $\Delta S(\tau)$, measured over a τ interval I_S of length T_S, is calculated by

$$\mathrm{RMS}^2 = \frac{1}{T_S}\int_{I_S} {\rm d}\tau\,\Delta S^2(\tau) - \frac{1}{T_0}\int_{I_0} {\rm d}\tau\,\Delta S^2(\tau). \tag{B3}$$

Here, the second term on the right-hand side subtracts the noise contribution, which is estimated by the signal RMS over a τ interval I_0 of length T_0 in which the signal is absent and, thus, dominated by noise. Typically, we choose τ intervals before arrival of the pump pulse ($\tau < 0$).

4. Amplitude relative to a reference

To obtain the relative amplitude A of a signal waveform $\Delta S(\tau)$, measured over a time interval I_S, with respect to a reference signal $\Delta S_{\rm ref}(\tau)$ on the same time interval, we simply project ΔS on $\Delta S_{\rm ref}$ by the linear correlation factor [55]

$$A = \frac{\int_{I_S}{\rm d}\tau\,\Delta S(\tau)\Delta S_{\rm ref}(\tau)}{\int_{I_S}{\rm d}\tau\,\Delta S^2_{\rm ref}(\tau)}. \tag{B4}$$

First, this method is linear with respect to ΔS and, thus, conserves the relative sign of ΔS, in contrast to RMS [Eq. (B3)]. Second, it accounts for all sampled points, as opposed to one-point measures, such as the maximum value. Finally, it is less sensitive to signal contributions that do not follow the temporal dynamics of the reference $\Delta S_{\rm ref}$.

5. Extraction of domain statistics

To obtain the domain volume fractions shown in Fig. 7(d), we combine various observables as follows. First, the domain contribution $\alpha := f_{0^\circ} + f_{180^\circ}$ is obtained from the quasistatic data $\langle R_0^+\rangle$ according to Eq. (22). Second, $\beta := f_{0^\circ} - f_{180^\circ}$ and $\gamma := f_{90^\circ} - f_{270^\circ}$ are obtained from the pump-probe signals $\langle\Delta Q^-\rangle/\langle\Delta Q^-\rangle|_{\rm sat}$ for $\boldsymbol{E}\parallel\boldsymbol{u}_x$ and $\boldsymbol{E}\parallel\boldsymbol{u}_y$, respectively [Eq. (28)].

It follows that $f_{0^\circ} = (\alpha+\beta)/2$, $f_{180^\circ} = (\alpha-\beta)/2$, $f_{90^\circ} = (1-\alpha+\gamma)/2$ and, finally, $f_{270^\circ} = 1-(f_{0^\circ}+f_{90^\circ}+f_{270^\circ})$.

6. Calibration of torkance

In the frequency domain, the amplitude E of the linearly polarized THz electric field inside the film between two homogeneous half-spaces is given by the Tinkham equation [41]

$$\frac{E}{E_{\rm inc}} = \frac{2n_1}{n_1+n_2+Z_0/R_{\rm s}}. \tag{B5}$$

Here, $E_{\rm inc}$ is the incident field, n_1 and n_2 is the refractive index of the first half-space (air, $n_1=1$) and the second half-space (MgO, $n_2\approx 3$), respectively. Further, Z_0 is the vacuum impedance, and $R_{\rm s}$ is the sheet resistance of the metal film.

In the time domain, the linear response of the Néel vector to E is determined by $\Delta\varphi_L = AH_{\Delta\varphi_L\leftarrow E_x} * E$, where the impulse response function $H_{\Delta\varphi_L\leftarrow E_x}$ [Eq. (9)] is given in Table II. The coefficient A depends on the torkance $\lambda_{\rm NSOT}$ [14,42] through

$$A = \gamma B_{\rm ex}\sigma\lambda_{\rm NSOT}. \tag{B6}$$

We use the fit result shown in Fig. 5(a), the amplitude calibration (Sec. III B 5) and $\sigma = 1/R_s d = 8.8$ MS m^{-1}, as obtained from the measured $R_s = 1.2\ \Omega$ and the total metal-film thickness of $d = 93$ nm. We obtain $A \approx 2.1 \times 10^7$ m V^{-1} s^{-1} and $\lambda_{\mathrm{NSOT}} \approx 90$ cm^2 A^{-1} s^{-1}, where Eq. (46) and the literature value of $B_{\mathrm{ex}} = 1300$ T [21] were used.

[1] T. Jungwirth, X. Marti, P. Wadley, and J. Wunderlich, Antiferromagnetic spintronics, Nat. Nanotechnol. **11**, 231 (2016).

[2] S. Schlauderer, C. Lange, S. Baierl, T. Ebnet, C. P. Schmid, D. C. Valovcin, A. K. Zvezdin, A. V. Kimel, R. V. Mikhaylovskiy, and R. Huber, Temporal and spectral fingerprints of ultrafast all-coherent spin switching, Nature (London) **569**, 383 (2019).

[3] C. Tzschaschel, T. Satoh, and M. Fiebig, Tracking the ultrafast motion of an antiferromagnetic order parameter, Nat. Commun. **10**, 3995 (2019).

[4] A. S. Disa, M. Fechner, T. F. Nova, B. Liu, M. Först, D. Prabhakaran, P. G. Radaelli, and A. Cavalleri, Polarizing an antiferromagnet by optical engineering of the crystal field, Nat. Phys. **16**, 937 (2020).

[5] E. A. Mashkovich, K. A. Grishunin, R. M. Dubrovin, A. K. Zvezdin, R. V. Pisarev, and A. V. Kimel, Terahertz light-driven coupling of antiferromagnetic spins to lattice, Science **374**, 1608 (2021).

[6] Z. Zhang, M. Kanega, K. Maruyama, T. Kurihara, M. Nakajima, T. Tachizaki, M. Sato, Y. Kanemitsu, and H. Hirori, Spin switching in $Sm_{0.7}Er_{0.3}FeO_3$ triggered by terahertz magnetic-field pulses, Nat. Mater. **24**, 219 (2024).

[7] R. A. Leenders, D. Afanasiev, A. V. Kimel, and R. V. Mikhaylovskiy, Canted spin order as a platform for ultrafast conversion of magnons, Nature (London) **630**, 335 (2024).

[8] J. Železný, H. Gao, K. Výborný, J. Zemen, J. Mašek, A. Manchon, J. Wunderlich, J. Sinova, and T. Jungwirth, Relativistic Néel-order fields induced by electrical current in antiferromagnets, Phys. Rev. Lett. **113**, 157201 (2014).

[9] P. Wadley, B. Howells, J. Železný, C. Andrews, V. Hills, R. P. Campion, V. Novák, K. Olejník, F. Maccherozzi, S. S. Dhesi, *et al.*, Electrical switching of an antiferromagnet, Science **351**, 587 (2016).

[10] S. Y. Bodnar, L. Šmejkal, I. Turek, T. Jungwirth, O. Gomonay, J. Sinova, A. A. Sapozhnik, H. J. Elmers, M. Kläui, and M. Jourdan, Writing and reading antiferromagnetic Mn_2Au by Néel spin-orbit torques and large anisotropic magnetoresistance, Nat. Commun. **9**, 348 (2018).

[11] K. Olejník, T. Seifert, Z. Kašpar, V. Novák, P. Wadley, R. P. Campion, M. Baumgartner, P. Gambardella, P. Němec, J. Wunderlich, *et al.*, Terahertz electrical writing speed in an antiferromagnetic memory, Sci. Adv. **4**, eaar3566 (2018).

[12] X. Chen, X. Zhou, R. Cheng, C. Song, J. Zhang, Y. Wu, Y. Ba, H. Li, Y. Sun, Y. You, *et al.*, Electric field control of Néel spin–orbit torque in an antiferromagnet, Nat. Mater. **18**, 931 (2019).

[13] S. Reimers, Y. Lytvynenko, Y. R. Niu, E. Golias, B. Sarpi, L. S. I. Veiga, T. Denneulin, A. Kovács, R. E. Dunin-Borkowski, J. Bläßer, *et al.*, Current-driven writing process in antiferromagnetic Mn_2Au for memory applications, Nat. Commun. **14**, 1861 (2023).

[14] Y. Behovits, A. L. Chekhov, S. Y. Bodnar, O. Gueckstock, S. Reimers, Y. Lytvynenko, Y. Skourski, M. Wolf, T. S. Seifert, O. Gomonay, *et al.*, Terahertz Néel spin-orbit torques drive nonlinear magnon dynamics in antiferromagnetic Mn_2Au, Nat. Commun. **14**, 6038 (2023).

[15] H. Al-Hamdo, T. Wagner, Y. Lytvynenko, G. Kendzo, S. Reimers, M. Ruhwedel, M. Yaqoob, V. I. Vasyuchka, P. Pirro, J. Sinova, *et al.*, Coupling of ferromagnetic and antiferromagnetic spin dynamics in Mn_2Au|NiFe thin film bilayers, Phys. Rev. Lett. **131**, 046701 (2023).

[16] S. P. Bommanaboyena, D. Backes, L. S. I. Veiga, S. S. Dhesi, Y. R. Niu, B. Sarpi, T. Denneulin, A. Kovács, T. Mashoff, O. Gomonay, *et al.*, Readout of an antiferromagnetic spintronics system by strong exchange coupling of Mn_2Au and Permalloy, Nat. Commun. **12**, 6539 (2021).

[17] See Supplemental Material at http://link.aps.org/supplemental/10.1103/86ds-j6vv for electric field characterization, raw data of the waveforms, fitting parameters, alternative fitting method, and balanced detection schematic.

[18] R. Rouzegar, A. L. Chekhov, Y. Behovits, B. R. Serrano, M. A. Syskaki, C. H. Lambert, D. Engel, U. Martens, M. Münzenberg, M. Wolf, *et al.*, Broadband spintronic terahertz source with peak electric fields exceeding 1.5 MV/cm, Phys. Rev. Appl. **19**, 034018 (2023).

[19] A. L. Chekhov, Y. Behovits, U. Martens, B. R. Serrano, M. Wolf, T. S. Seifert, M. Münzenberg, and T. Kampfrath, Broadband spintronic detection of the absolute field strength of terahertz electromagnetic pulses, Phys. Rev. Appl. **20**, 034037 (2023).

[20] S. F. Maehrlein, I. Radu, P. Maldonado, A. Paarmann, M. Gensch, A. M. Kalashnikova, R. V. Pisarev, M. Wolf, P. M. Oppeneer, J. Barker, *et al.*, Dissecting spin-phonon equilibration in ferrimagnetic insulators by ultrafast lattice excitation, Sci. Adv. **4**, eaar5164 (2018).

[21] V. M. T. S. Barthem, C. V. Colin, H. Mayaffre, M. H. Julien, and D. Givord, Revealing the properties of Mn_2Au for antiferromagnetic spintronics, Nat. Commun. **4**, 2892 (2013).

[22] V. Grigorev, M. Filianina, S. Y. Bodnar, S. Sobolev, N. Bhattacharjee, S. Bommanaboyena, Y. Lytvynenko, Y. Skourski, D. Fuchs, M. Kläui, *et al.*, Optical readout of the Néel vector in the metallic antiferromagnet Mn_2Au, Phys. Rev. Appl. **16**, 014037 (2021).

[23] X. Fan, A. R. Mellnik, W. Wang, N. Reynolds, T. Wang, H. Celik, V. O. Lorenz, D. C. Ralph, and J. Q. Xiao, All-optical vector measurement of spin-orbit-induced torques using both polar and quadratic magneto-optic Kerr effects, Appl. Phys. Lett. **109**, 122406 (2016).

[24] R. Silber, O. Stejskal, L. Beran, P. Cejpek, R. Antoš, T. Matalla-Wagner, J. Thien, O. Kuschel, J. Wollschläger, M. Veis, *et al.*, Quadratic magneto-optic Kerr effect spectroscopy of Fe epitaxial films on MgO(001) substrates, Phys. Rev. B **100**, 064403 (2019).

[25] R. Lopusnik, J. P. Nibarger, T. J. Silva, and Z. Celinski, Different dynamic and static magnetic anisotropy in thin Permalloy films, Appl. Phys. Lett. **83**, 96 (2003).

[26] J. Hamrle, S. Blomeier, O. Gaier, B. Hillebrands, H. Schneider, G. Jakob, K. Postava, and C. Felser, Huge quadratic magneto-optical Kerr effect and magnetization reversal in the Co_2FeSi Heusler compound, J. Phys. D Appl. Phys. **40**, 1563 (2007).

[27] C. Vicario, C. Ruchert, F. Ardana-Lamas, P. M. Derlet, B. Tudu, J. Luning, and C. P. Hauri, Off-resonant magnetization dynamics phase-locked to an intense phase-stable terahertz transient, Nat. Photon. **7**, 720 (2013).

[28] K. Neeraj, N. Awari, S. Kovalev, D. Polley, N. Zhou Hagström, S. S. P. K. Arekapudi, A. Semisalova, K. Lenz, B. Green, J.-C. Deinert, *et al.*, Inertial spin dynamics in ferromagnets, Nat. Phys. **17**, 245 (2021).

[29] T. Kampfrath, A. Sell, G. Klatt, A. Pashkin, S. Mährlein, T. Dekorsy, M. Wolf, M. Fiebig, A. Leitenstorfer, and R. Huber, Coherent terahertz control of antiferromagnetic spin waves, Nat. Photon. **5**, 31 (2011).

[30] M. Arana, F. Estrada, D. S. Maior, J. B. S. Mendes, L. E. Fernandez-Outon, W. A. A. Macedo, V. M. T. S. Barthem, D. Givord, A. Azevedo, and S. M. Rezende, Observation of magnons in Mn_2Au films by inelastic Brillouin and Raman light scattering, Appl. Phys. Lett. **111**, 192409 (2017).

[31] M. Weißenhofer, F. Foggetti, U. Nowak, and P. M. Oppeneer, Néel vector switching and terahertz spin-wave excitation in Mn_2Au due to femtosecond spin-transfer torques, Phys. Rev. B **107**, 174424 (2023).

[32] I. V. Bar'yakhtar and B. A. Ivanov, Nonlinear waves in antiferromagnets, Solid State Commun. **34**, 545 (1980).

[33] B. A. Ivanov, Spin dynamics for antiferromagnets and ultrafast spintronics, J. Exp. Theor. Phys. **131**, 95 (2020).

[34] O. Gomonay, V. Baltz, A. Brataas, and Y. Tserkovnyak, Antiferromagnetic spin textures and dynamics, Nat. Phys. **14**, 213 (2018).

[35] A. L. Chekhov, Y. Behovits, J. J. F. Heitz, C. Denker, D. A. Reiss, M. Wolf, M. Weinelt, P. W. Brouwer, M. Münzenberg, and T. Kampfrath, Ultrafast demagnetization of iron induced by optical versus terahertz pulses, Phys. Rev. X **11**, 041055 (2021).

[36] B. Koopmans, M. van Kampen, J. T. Kohlhepp, and W. J. M. de Jonge, Ultrafast magneto-optics in nickel: Magnetism or optics? Phys. Rev. Lett. **85**, 844 (2000).

[37] T. Kampfrath, R. G. Ulbrich, F. Leuenberger, M. Münzenberg, B. Sass, and W. Felsch, Ultrafast magneto-optical response of iron thin films, Phys. Rev. B **65**, 104429 (2002).

[38] M. C. Hoffmann, N. C. Brandt, H. Y. Hwang, K.-L. Yeh, and K. A. Nelson, Terahertz Kerr effect, Appl. Phys. Lett. **95**, 231105 (2009).

[39] M. Sajadi, M. Wolf, and T. Kampfrath, Terahertz-field-induced optical birefringence in common window and substrate materials, Opt. Express **23**, 28985 (2015).

[40] S. Baierl, J. H. Mentink, M. Hohenleutner, L. Braun, T.-M. Do, C. Lange, A. Sell, M. Fiebig, G. Woltersdorf, T. Kampfrath, *et al.*, Terahertz-driven nonlinear spin response of antiferromagnetic nickel oxide, Phys. Rev. Lett. **117**, 197201 (2016).

[41] L. Nádvorník, M. Borchert, L. Brandt, R. Schlitz, K. A. De Mare, K. Výborný, I. Mertig, G. Jakob, M. Kläui, S. T. B. Goennenwein, *et al.*, Broadband terahertz probes of anisotropic magnetoresistance disentangle extrinsic and intrinsic contributions, Phys. Rev. X **11**, 021030 (2021).

[42] O. Gomonay, T. Jungwirth, and J. Sinova, Narrow-band tunable terahertz detector in antiferromagnets via staggered-field and antidamping torques, Phys. Rev. B **98**, 104430 (2018).

[43] T. Kuschel, H. Bardenhagen, H. Wilkens, R. Schubert, J. Hamrle, J. Pištora, and J. Wollschläger, Vectorial magnetometry using magnetooptic Kerr effect including first- and second-order contributions for thin ferromagnetic films, J. Phys. D Appl. Phys. **44**, 265003 (2011).

[44] O. Gomonay and D. Bossini, Linear and nonlinear spin dynamics in multi-domain magnetoelastic antiferromagnets, J. Phys. D Appl. Phys. **54**, 374004 (2021).

[45] H. Meer, O. Gomonay, C. Schmitt, R. Ramos, L. Schnitzspan, F. Kronast, M.-A. Mawass, S. Valencia, E. Saitoh, J. Sinova, *et al.*, Strain-induced shape anisotropy in antiferromagnetic structures, Phys. Rev. B **106**, 094430 (2022).

[46] L. Šmejkal, J. Sinova, and T. Jungwirth, Emerging research landscape of altermagnetism, Phys. Rev. X **12**, 040501 (2022).

[47] S. F. Weber, A. Urru, S. Bhowal, C. Ederer, and N. A. Spaldin, Surface magnetization in antiferromagnets: Classification, example materials, and relation to magnetoelectric responses, Phys. Rev. X **14**, 021033 (2024).

[48] M. Fiebig, D. Fröhlich, G. Sluyterman v. L., and R. V. Pisarev, Domain topography of antiferromagnetic Cr_2O_3 by second-harmonic generation, Appl. Phys. Lett. **66**, 2906 (1995).

[49] B. Zhang, Z. Ma, J. Ma, X. Wu, C. Ouyang, D. Kong, T. Hong, X. Wang, P. Yang, L. Chen, *et al.*, 1.4-mJ high energy terahertz radiation from lithium niobates, Laser and Photonics Reviews **15**, 2000295 (2021).

[50] L. Tesi, D. Bloos, M. Hrtoň, A. Beneš, M. Hentschel, M. Kern, A. Leavesley, R. Hillenbrand, V. Křápek, T. Šikola, *et al.*, Plasmonic metasurface resonators to enhance terahertz magnetic fields for high-frequency electron paramagnetic resonance, Small Methods **5**, 2100376 (2021).

[51] Y. Behovits, A. L. Chekhov, B. Rosinus Serrano, A. Ruge, S. Reimers, Y. Lytvynenko, M. Kläui, M. Jourdan, and T. Kampfrath, Data for Behovits *et al.* "All-optical magnetometric characterization of the exchange-coupled antiferromagnet|ferromagnet system $Mn_2Au|Ni_{80}Fe_{20}$ by terahertz spin-orbit torques", [Data set] Zenodo, https://doi.org/10.5281/zenodo.19651386 (2026).

[52] D. L. Mills, *Nonlinear Optics* (Springer, Berlin, Heidelberg, 1998).

[53] L. Novotny and B. Hecht, *Principles of Nano-Optics*, 2nd ed. (Cambridge University Press, Cambridge, 2012).

[54] A. Hubert and G. Traeger, Magneto-optical sensitivity functions of thin-film systems, J. Magn. Magn. Mater. **124**, 185 (1993).

[55] L. Braun, G. Mussler, A. Hruban, M. Konczykowski, T. Schumann, M. Wolf, M. Münzenberg, L. Perfetti, and T. Kampfrath, Ultrafast photocurrents at the surface of the three-dimensional topological insulator Bi_2Se_3, Nat. Commun. **7**, 13259 (2016).